

Herschel far-infrared photometry of the Swift Burst Alert Telescope active galactic nuclei sample of the local universe—III. Global star-forming properties and the connection to nuclear activity[★]

T. Taro Shimizu^{1†}, Richard F. Mushotzky¹, Marcio Meléndez^{1,2,3}, Michael J. Koss⁴, Amy J. Barger^{5,6,7}, and Lennox L. Cowie⁷

¹Department of Astronomy, University of Maryland, College Park, MD 20742, USA

²NASA Goddard Space Flight Center, Greenbelt, MD 20771, USA

³KBRwyle Science, Technology and Engineering Group, 1290 Hercules Avenue Houston, TX 77058, USA

⁴Institute for Astronomy, Department of Physics, ETH Zurich, Wolfgang-Pauli-Strasse 27, CH-8093 Zurich, Switzerland

⁵Department of Astronomy, University of Wisconsin-Madison, 475 N. Charter Street, Madison, WI 53706, USA

⁶Department of Physics and Astronomy, University of Hawaii, 2505 Correa Road, Honolulu, HI 96822, USA

⁷Institute for Astronomy, University of Hawaii, 2680 Woodlawn Drive, Honolulu, HI 96822, USA

Accepted XXX. Received YYY; in original form ZZZ

ABSTRACT

~~In the third paper of this series,~~ we combine the *Herschel Space Observatory* PACS and SPIRE photometry with archival *WISE* photometry to construct the spectral energy distributions (SED) for over 300 local ($z < 0.05$), ultra-hard X-ray (14–195 keV) selected active galactic nuclei (AGN) from the *Swift Burst Alert Telescope* (BAT) 58 month catalogue. Using a simple analytical model that combines an exponentially cut-off powerlaw with a single temperature modified blackbody, we decompose the SEDs into a host-galaxy and AGN component. Based on our modeling, we calculate dust masses, dust temperatures, and star-formation rates (SFR) for our entire sample and compare them to a stellar mass-matched sample of local non-AGN galaxies. We find AGN host galaxies systematically higher dust masses, dust temperatures, and SFRs due to the higher prevalence of late-type galaxies to host an AGN in agreement with previous studies of the *Swift*/BAT AGN. We provide a scaling to convert X-ray luminosities into 8–1000 μm AGN luminosities as well as conversions from various mid-far infrared colors to the AGN-to-host galaxy ratio within 8–1000 μm . We find that for nearly 30 per cent of our sample, the 70 μm emission contains a significant contribution from the AGN (> 0.5), especially at higher luminosities ($L_{14-195\text{ keV}} > 10^{42.5}$). Finally, we measure the local SFR-AGN luminosity relationship, finding a slope of 0.18, large scatter (0.37 dex), and no evidence for an upturn at high AGN luminosity. We conclude with a discussion on the implications of our results within the context of galaxy evolution with and without AGN feedback.

Key words: galaxies: active – galaxies: Seyfert – infrared: galaxies – galaxies: star formation – galaxies: evolution

1 INTRODUCTION

Ever since the discoveries that the large scale properties of galaxies are related to the mass of the supermassive black

holes (SMBH) they host (Magorrian et al. 1998; Ferrarese & Merritt 2000; Gebhardt et al. 2000; Marconi & Hunt 2003; Häring & Rix 2004; Gültekin et al. 2009; McConnell & Ma 2013; Kormendy & Ho 2013), studies have intensely focused on finding the link between the evolution and growth of both the galaxy and SMBH. Theoretical arguments (eg. Silk & Rees 1998) as well as cosmological simulations (e.g. Croton et al. 2006; Bower et al. 2006) support the idea that SMBHs, while accreting material in their active galactic nuclei (AGN)

[★] *Herschel* is an ESA space observatory with science instruments provided by European-led Principal Investigator consortia and with important participation from NASA.

[†] Email: tshimizu@astro.umd.edu

phase, can affect both their own growth and the growth of their host galaxy through a mechanism that shuts down accretion and star formation (i.e. negative feedback).

Early evidence backing this theory seemed to be found in the observation that the SFR density and accretion rate density of the universe evolve similarly with redshift (Boyle & Terlevich 1998; Franceschini et al. 1999; Silverman et al. 2008, 2009; Aird et al. 2010; Merloni & Heinz 2013). Further, AGN host galaxies were found to predominantly lie in the “green valley” of the color-magnitude diagram, in between the blue, star-forming galaxies and “red-and-dead” quiescent ones (Martin et al. 2007; Nandra et al. 2007; Silverman et al. 2008; Schawinski et al. 2010; Koss et al. 2011), suggesting that nuclear activity plays a role in transitioning its host galaxy from star-forming to quiescence.

While suggestive, optical colors can be strongly affected by extinction due to dust that might move a galaxy from “blue” to “green” (Cardamone et al. 2010). Other measures of the SFR including emission line, ultra-violet (UV), and mid-infrared (MIR) luminosities that are extensively used for normal, non-AGN galaxies suffer from varying degrees of contamination in the presence of an AGN, especially unabsorbed ($N_{\text{H}} < 10^{22} \text{ cm}^{-2}$) Type I AGN.

This problem was solved with the advent of far-infrared (FIR; $\lambda = 40 - 500 \mu\text{m}$) telescopes, including the *Infrared Astronomical Satellite* (IRAS), the *Infrared Space Observatory* (ISO), the *Spitzer Space Telescope*, and most recently the *Herschel Space Observatory* (Pilbratt et al. 2010). FIR emission remains the ideal waveband to study star formation in AGN host galaxies for two reasons: (1) the rapidly declining spectral energy distribution (SED) associated with AGN heated dust in the FIR regime (Fritz et al. 2006; Netzer et al. 2007; Mullaney et al. 2011; Shi et al. 2014) ensures little AGN contamination (2) thermal emission of large grains heated by the ionizing emission of recently formed massive stars (Lonsdale Persson & Helou 1987; Devereux & Young 1990) creates a strong FIR “bump” and provides a reliable measure of the recent (10–100 Myr) SFR (Kennicutt 1998).

Even though the FIR can provide a reliable SFR tracer, individual investigations into the connection between AGN activity and star-formation have produced conflicting and even contradictory results. Some studies (Page et al. 2012; Barger et al. 2015) have reported lowered SFRs for the highest luminosity AGN, indicative of a suppression of star formation due to AGN feedback. Others have found weak or flat relationships (Diamond-Stanic & Rieke 2012; Mullaney et al. 2012; Rovilos et al. 2012; Rosario et al. 2012; Azadi et al. 2015; Stanley et al. 2015) especially at more moderate AGN luminosities. Finally, some find an overall positive correlation (Lutz et al. 2008; Netzer 2009; Rovilos et al. 2012; Rosario et al. 2012; Chen et al. 2013; Dai et al. 2015).

Many of the studies possibly however suffer from one or more problems that include small number statistics either due to a small area survey or low sensitivity, an inaccurate scaling from monochromatic luminosities to a total SFR, and source confusion due to the relatively large beam size of *Herschel*, especially at longer wavelengths.

In this paper, we aim to test these findings on the AGN-star formation relationship in the low redshift universe. We have performed a *Herschel* survey of a sample of AGN from the *Swift* Burst Alert Telescope 58 month catalogue which selected sources over the entire sky in the 14–195 keV en-

ergy range. At this high of energy, we are nearly unbiased with respect to any host galaxy properties including SFR as well as obscuration below a hydrogen column density (N_{H}) of 10^{24} cm^{-2} . The *Swift*/BAT AGN sample has been extensively studied since the release of the first 9-month catalogue (?). Most relevant to our work, Koss et al. (2011) performed an optical survey of over 100 AGN using combined *Sloan Digital Sky Survey* (SDSS) and *Kitt Peak National Observatory* imaging to study their host galaxy properties. They found that the *Swift*/BAT AGN are dominated by massive ($M_{\text{star}} > 10^{9.5} M_{\odot}$) spirals with bluer colors than a mass-matched sample of non-AGN galaxies. Koss et al. (2011) further found that AGN showed enhanced FIR luminosities, using 90 μm photometry from *Akari*.

With 5 band imaging with *Herschel* along with archival photometry from the *Wide-field Infrared Survey Explorer* (*WISE*), we have constructed MIR-FIR SEDs for over 300 AGN, allowing us to accurately measure the SFR in a robust manner. Because of the low-redshift nature of our sources, every AGN is easily able to be identified and there is no concern over source confusion. These SEDs not only allow us to calculate SFRs but also to test varying SED decomposition methods and models as well as measure other properties of the host galaxies such as the dust mass and dust temperature to compare with non-AGN samples. With a high detection rate (95, 83, 86, 72, and 46 per cent at 70, 160, 250, 350, and 500 μm), our measured properties from the SEDs are well constrained, removing much of the uncertainty due to censoring.

The paper is organized as follows: in Section 2 we briefly describe the *Herschel*-BAT AGN sample; in Section 3 we detail our *WISE* and *Herschel* datasets. Section 4 introduces our non-AGN comparison sample. Section 5 qualitatively examines the SEDs and determines calculates the average SED as a function of AGN luminosity, while Section 6 outlines our fitting methods. Sections 7 and 8 then discuss our results, compares with other studies, and concludes the paper. Throughout, we use a cosmology with $H_0 = 70 \text{ km s}^{-1} \text{ Mpc}^{-1}$, $\Omega_{\text{M}} = 0.3$, and $\Omega_{\Lambda} = 0.7$ to calculate luminosity distances from redshifts.

2 *Herschel*-BAT SAMPLE

Because *Swift*/BAT continuously monitors the entire sky in the energy range 14–195 keV for gamma ray bursts, it simultaneously provides an all-sky survey at ultra high X-ray energies. This allows for the creation of complete catalogues with increasing sensitivity the longer *Swift*/BAT remains in operation. Given the extreme environments necessary to produce strong 14–195 keV emission, the majority of sources in the *Swift*/BAT catalogues are AGN.

We chose 313 AGN from the parent sample of ~ 720 AGN detected in the 58 month catalogue¹ after imposing a redshift cutoff of $z < 0.05$ and excluding Blazars and BL Lac objects to form our *Herschel*-BAT AGN sample. With a mean redshift of $\langle z \rangle = 0.025$, our AGN sample provides a comprehensive view of the properties of AGN host

¹ <https://swift.gsfc.nasa.gov/results/bs58mon>

galaxies in the local universe. Our selection at ultra high X-ray energies further removes biases and selection effects due to host galaxy contamination and obscuration (Mushotzky 2004) that can influence samples at other wavelengths.

The demographics of our sample are nearly evenly split between Type I (43 per cent) and Type II (53 per cent) with the remaining 4 per cent (5 objects) either a Low-Ionization Nuclear Emission-line Region (LINER) or unclassified. The *Herschel*-BAT sample spans nearly four orders of magnitude in 14–195 keV luminosity ($10^{41} < L_{14-195\text{ keV}} < 10^{45}$ ergs s⁻¹) allowing for a robust determination of the connection between AGN strength and SFR. For a complete listing of our sample with names, luminosity distances, redshifts, and AGN type, we point the reader to Meléndez et al. (2014) or Shimizu et al. (2016).

3 DATA

3.1 *Herschel* Photometry

293 of the *Herschel*-BAT AGN were observed with *Herschel* as part of a Cycle 1 open time program (OT1_rmmushotz_1, PI: Richard Mushotzky). The remaining 20 sources were part of the other programs with public archival data. *Herschel* observed all 313 AGN using both the Photoconductor Array Camera and Spectrometer (PACS; Poglitsch et al. 2010) and Spectral and Photometric Imaging Receiver (SPIRE; Griffin et al. 2010) producing images in five wavebands: 70, 160, 250, 350, and 500 μm .

Detailed descriptions of the data reduction process and photometric flux extraction can be found in Meléndez et al. (2014) for PACS and Shimizu et al. (2016) for SPIRE. The following is a short description of the flux extraction procedure. We measured fluxes at each waveband directly from the images using aperture photometry with a concentric annulus to define the local background. We applied aperture corrections for sources where we used a point source aperture as defined in the respective PACS and SPIRE data reduction guides. Fluxes for sources that were unresolved at all three wavebands in SPIRE were determined using the SPIRE Timeline Fitter within the *Herschel* Interactive Processing Environment. All fluxes have a signal-to-noise ratio of at least 5, otherwise we provided a 5σ upper limit.

In Shimizu et al. (2016), using the SPIRE flux ratios, we found 6 radio-loud objects which have a large contribution to their FIR emission from synchrotron radiation due to their jets. These sources are Pictor A, 3C 111.0, 3C 120, 2MASX J23272195+1524375, PKS2331-240, and [HB89] 0241+622. For this work we remove these sources from all analysis, however we still provide figures of their SED fits in Appendix D and list their best-fit parameters in Table 1.

Also in Shimizu et al. (2016), we flagged objects with a “D” that likely had strong contamination due to a nearby source. For these sources, we treat the SPIRE fluxes as upper limits. For a small number of very nearby galaxies with large angular size (NGC 2655, NGC 3718, NGC 4939, NGC 4941, NGC 5033, and NGC 6300), we realized that the PACS FOV of our observations did not encompass the entirety of the galaxy leading to possible underestimations of the 70 and 160 μm flux densities. Therefore, for this work, we chose to conservatively increase the uncertainty to 50 per cent.

3.2 *WISE* Photometry

To extend the SEDs into the mid-infrared (MIR), we supplemented our *Herschel* data with archival *Wide-field Infrared Survey Explorer* (WISE; Wright et al. 2010) photometry. WISE performed a broadband all-sky survey at 3.4 (W1), 4.6 (W2), 12 (W3), and 22 (W4) μm with angular resolution comparable to *Herschel*/PACS at 70 μm for W1, W2, and W3 and 160 μm for W4. We queried the AllWISE catalogue through the NASA/IPAC Infrared Science Archive² to search for coincident sources within 6". Counterparts were found for all but one AGN (Mrk 3) at every waveband. The catalogue only contained W1 and W2 fluxes for Mrk 3 due to differences in the depth of coverage for W1/W2 and W3/W4, therefore Mrk 3 is not included as part of the sample in this work.

The AllWISE catalogue provides magnitudes determined using multiple extraction methods. We consider only the profile-fitting magnitudes (wN_{mpro} where N is 1, 2, 3, or 4) and the elliptical aperture magnitudes (wN_{mag}). Profile-fitting magnitudes were determined by fitting the position dependent point spread function using deblending procedures when necessary to decompose overlapping sources. The wN_{mpro} magnitudes therefore are only relevant for unresolved sources.

If a WISE source is associated with a source in the *Two Micron All Sky Survey* (2MASS) Extended Source Catalog (XSC), then wN_{mag} magnitudes were also measured using an elliptical aperture with the same shape from the XSC and sizes scaled given the larger WISE beam. Thus, wN_{mag} magnitudes are more appropriate for extended sources. For details of all of the WISE magnitude measurements we point the reader to the All-Sky Release Explanatory Supplement³.

Given the low-redshift nature of our sample, using only the wN_{mpro} magnitudes would severely underestimate the flux for large extended sources. To decide which magnitude to include in the SED for each source, we used the reduced χ^2 value (wN_{rchi2}) from the profile-fitting. If $wN_{\text{rchi2}} < 3$ then we chose the wN_{mpro} magnitude, otherwise wN_{mag} was chosen.



4 COMPARISON SAMPLE

To test whether the AGN has any effect on the star-forming properties of their host galaxies, we need samples of galaxies which contain little evidence for nuclear activity. These samples also need to occupy the same redshift range to mitigate against evolutionary effects and have been observed with nearly the same instruments so the properties can be compared on an equal level. Three low-redshift samples exist that satisfy these constraints. They are the *Herschel Reference Survey* (HRS; Boselli et al. 2010), *Key Insights on Nearby Galaxies: a Far-Infrared Survey with Herschel* (KINGFISH; Kennicutt et al. 2011), and the *Herschel Stripe 82 Survey* (HerS; Viero et al. 2014). While the KINGFISH sample has been observed with at all of the same wavelengths as the *Herschel*-BAT AGN, the sample was selected

² <http://irsa.ipac.caltech.edu/frontpage/>

³ <http://wise2.ipac.caltech.edu/docs/release/allsky/expsup/>

in a heterogeneous manner and only contains 61 galaxies that does not allow for stellar mass matching. The HRS sample is numerous and covers a large range in mass, however was only observed with SPIRE. Further, the catalog was built based on SPIRE detections which imposes a selection effect associated with the SFR. We therefore chose the HRS as our comparison sample to the *Herschel*-BAT AGN.

The HRS was a guaranteed time key *Herschel* program dedicated to studying the dust content of “normal” galaxies. The 323 galaxy sample is volume limited ($15 < D < 25$ Mpc) to avoid distance effects and K-band flux limited to avoid selection effects due to dust and provide a representative population of local galaxies. The size of the HRS as well as the local nature make it an ideal sample to compare to the *Herschel*-BAT galaxies.

The HRS galaxies also were imaged using both PACS and SPIRE, although the $100\ \mu\text{m}$ filter was used instead of the $70\ \mu\text{m}$ filter. Cortese et al. (2014) and Ciesla et al. (2012) measured the PACS and SPIRE flux densities respectively using similar techniques as the *Herschel*-BAT galaxies. WISE 12 and $22\ \mu\text{m}$ photometry for HRS were provided in Ciesla et al. (2014). The available data for the HRS SEDs are nearly identical as our sample.

The only issue in comparing the HRS galaxies to the *Herschel*-BAT AGN concerns the stellar mass (M_{star}) distribution. Because the near-infrared is most strongly effected by the mass of the older stellar population, the HRS K-band selection produces a M_{star} distribution that is representative of the naturally occurring M_{star} distribution. However, many recent studies have shown that AGN prefer high M_{star} galaxies (e.g. Schawinski et al. 2010; Xue et al. 2010), a feature that is also found in the BAT AGN (Koss et al. 2011). Figure 1 displays the M_{star} distributions for the *Herschel*-BAT and HRS sample (dashed line). The *Herschel*-BAT galaxies have an average M_{star} of $10.6\ M_{\odot}$, whereas the average M_{star} for HRS is $9.8\ M_{\odot}$, nearly a ten-fold difference.

To account for possible stellar mass effects, we decided to produce a mass-matched HRS sample in the following way. Stellar masses for the *Herschel*-BAT AGN were calculated based on the AGN-subtracted *ugriz* photometry from (Koss et al. 2011) and the $g-i$ calibrated stellar mass relation from Zibetti et al. (2009). This is the same method that stellar masses were calculated for the HRS sample, given in Cortese et al. (2012b). For each of the 122 *Herschel*-BAT AGN which have stellar mass estimates, we chose all HRS galaxies which have a stellar mass within 0.15 dex of the *Herschel*-BAT mass. We then randomly selected an HRS galaxy from this pool. Because high-mass galaxies are relatively rare in the HRS sample, some matches are duplicated. We find though 97/122 of the matched HRS galaxies are unique, representing 80% of the sample so the duplicating effects should not be large. The red solid line in Figure 1 now shows the mass-matched HRS sample which overlaps with the *Herschel*-BAT mass distribution. Throughout the rest of this paper, we refer to the HRS mass-matched sample as simply the HRS sample unless otherwise noted.

5 THE IR SEDS OF $Z = 0$ AGN

Before fitting the SEDs and comparing to a non-AGN sample, we begin with a qualitative look at the SEDs of the

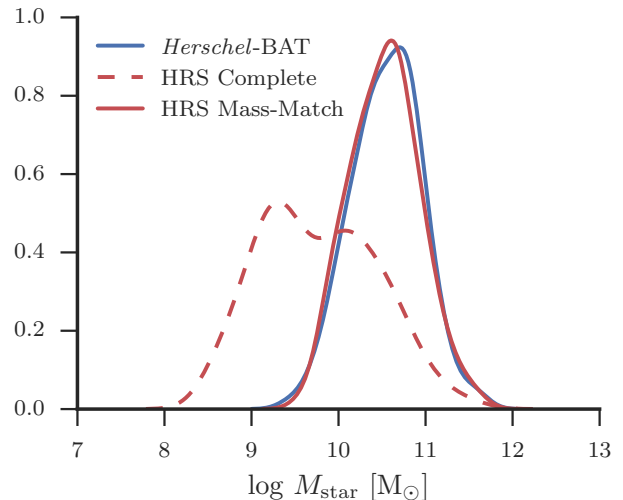


Figure 1. Kernel Density Estimates (KDE) of the M_{star} distribution for the BAT AGN (blue), full HRS sample (red), and mass-matched HRS sample (red dashed). The *Herschel*-BAT AGN probe a higher M_{star} galaxy population than the full samples, however with mass-matching we can reproduce the stellar-mass distribution of the *Herschel*-BAT AGN with non-AGN. A color version is available in the online publication.

313 AGN. Figure D1 shows the 12– $500\ \mu\text{m}$ SED for every source in the *Herschel*-BAT sample. Immediately noticeable is the varied SED shapes. Some of the SEDs (e.g. 2MASX J07595347+2323241, Cen A, ESO 005-G004, NGC 4051, NGC 4138, NGC 6814) feature a very prominent FIR bump that is recognizable in nearly all star-forming galaxies and is indicative of thermally heated dust from recently formed massive stars as well as cirrus emission heated by an older population. The general shape is usually well fit by a blackbody modified by a frequency dependent optical depth (e.g. Calzetti et al. 2000; Smith et al. 2012; Bianchi 2013; Symeonidis et al. 2013; Cortese et al. 2014).

These star formation dominated objects represent one extreme end of the shapes we observe. The other extreme are SEDs whose shapes seem to peak short-ward of $70\ \mu\text{m}$ and display rapidly falling emission with increasing wavelength. Examples include 2MASX J06561197-4919499, 2MASX J210990996-0940147, ESO 103-035, IC 4329A, MCG -05-23-016, and Mrk 335. Emission in the MIR dominates these SEDs and is likely associated with hotter dust heated by the AGN. MIR colors are commonly used to select AGN samples because they display strong red (i.e. increasing SED with wavelength) colors compared to non-AGN galaxies (Lacy et al. 2004; Donley et al. 2012; Stern et al. 2012) due to the dust in the obscuring torus heated by the optical and UV emission from the accretion disk. Monochromatic MIR luminosities, especially for sources dominated by an unresolved central component, show near linear correlations with the X-ray luminosity (e.g. Lutz et al. 2004; Gandhi et al. 2009; Asmus et al. 2012) providing more evidence that much of the MIR in AGN host galaxies is associated with the AGN.

The remaining *Herschel*-BAT AGN display SEDs somewhere in between MIR-dominated and FIR-dominated as

a result of competing contributions between the AGN and star formation. The varied shapes of the SED emphasizes the need for SED decomposition, especially at shorter wavelengths, to accurately determine the IR luminosity associated with either star formation or the AGN.

If star formation suppression occurs at high AGN luminosity then we expect the IR SEDs for the most X-ray luminous sources to resemble the MIR-dominated SEDs as Barger et al. (2015) observed. To test this, we binned the SEDs by logarithmic 14–195 keV luminosity. Five bins ($\log L_{14-195\text{ keV}} > 42.5$, $\log L_{14-195\text{ keV}} = 42.5-43.0$, $43.0-43.5$, $43.5-44.0$, and $\log L_{14-195\text{ keV}} > 44.0$) were chosen with 0.5 dex widths to ensure enough sources occupied each one. The number of sources in each bin is 22, 39, 94, 116, and 35.

We then calculated the median luminosity density within each X-ray luminosity bin. We used the ASURV (Feigelson & Nelson 1985) package which applies the principles of survival analysis to astronomical data. Information contained in the upper limits can be then included in the measurement of statistical properties of samples without biasing results towards brighter sources that are more likely to be detected. Specifically, ASURV calculates the non-parametric Kaplan-Meier product-limit (KMPL) estimator for a sample distribution. The KMPL estimator is an estimate of the survival function which is simply 1–CDF (cumulative distribution function). Using the KMPL, we calculate for each waveband the median luminosity density (50th percentile) and estimate the uncertainty using the 16th and 84th percentiles.

Figure 2 shows the median IR SED for sources in each X-ray luminosity bin. From visual inspection, the median SED as a function of X-ray luminosity seems to be driven more by an increasing MIR hot dust component. There does not seem to be any indication that star formation is being suppressed at the highest luminosities. The wavebands that show the largest change with X-ray luminosity are the MIR bands. At wavelengths longer than 160 μm , the SED shows no significant change, consistent with the correlations we measured in Meléndez et al. (2014) and Shimizu et al. (2016). If we make the assumption that the longer wavelengths are mainly associated with star-formation, then the lack of change indicates star-formation is unrelated to X-ray luminosity within the range probed by our sample. However, to definitively test this we need to decompose the SED into star-forming and AGN components to accurately calculate SFRs.

6 SED FITTING

Many models and templates exist in the literature to fit the broadband SEDs of galaxies. We chose a model that allowed us to both decompose the SED into star-forming and AGN components as well as provide estimates on the dust temperature and dust mass.

6.1 Casey 2012 Model

One of the most widely used models for fitting the FIR SED of galaxies is a single modified blackbody (MBB). The simple model consists of a normal, single temperature blackbody that represents isotropic dust emission combined with

a frequency dependent opacity given that dust is not a perfect blackbody. In the optically thin limit, the opacity can be approximated as a powerlaw, $\tau_\nu = (\nu/\nu_0)^\beta$. The form of the single modified blackbody for the flux density at each frequency is then

$$S(\nu) \propto \nu^\beta B_\nu(T_d) \quad (1)$$

where β is the spectral emissivity index and $B_\nu(T_d)$ is the standard Planck blackbody function for an object with temperature T_d . This simple model has been shown to fit well the prominent FIR bumps for large samples of star-forming galaxies and provides estimates of the dust temperature, dust mass, and SFR (e.g. Calzetti et al. 2000; Bianchi 2013; Cortese et al. 2014).

To calculate the dust mass, we must assume a particular dust absorption coefficient, κ_0 at a particular frequency, ν_0 . For this work, we assume $\kappa_0 = 0.192\text{ m}^2\text{ kg}^{-1}$ and $\nu_0 = 857\text{ GHz}$ (i.e. 350 μm) from Draine (2003). However, as Bianchi (2013) shows, by assuming a specific κ_0 , we must also fix the spectral emissivity index to the value used to measure κ_0 . In this work, we fix $\beta = 2.0$ to match the spectral emissivity index used by Draine (2003).⁴ The final full form of the single MBB model is then

$$S_{\text{MBB}}(\nu) = \frac{M_d \kappa_0}{D_L^2} \left(\frac{\nu}{\nu_0} \right)^\beta \frac{2h\nu^3}{c^2} \frac{1}{e^{h\nu/kT_d} - 1} \quad (2)$$

where M_d is the dust mass, D_L is the luminosity distance, c is the speed of light, h is the Planck constant, and k is the Boltzmann constant. The two free parameters then are M_d and T_d , the dust mass and dust temperature respectively.

The simple assumption that dust emission in the IR can be modeled with a single temperature blackbody works well for “normal” star-forming galaxies. However for galaxies with large amounts of hot dust either due to a compact starburst or central AGN, this assumption can quickly break down. To account for this hot dust we also fit our sample using the model described in Casey (2012, hereafter C12) which is the combination of a single MBB and an exponentially cutoff powerlaw. The C12 model takes the form

$$S_{\text{C12}}(\nu) = N_{\text{pl}} \left(\frac{\nu}{\nu_c} \right)^{-\alpha} e^{-\nu/\nu_c} + S_{\text{MBB}}(\nu) \quad (3)$$

where ν_c represents the turnover frequency and N_{pl} is a normalization constant. C12 illustrated using the *Great Origins All-Sky LIRG Survey* (GOALS) sample that this model provides better estimates of the cold dust temperature, dust mass, and IR luminosity compared to both a single temperature modified blackbody and template libraries.

The C12 model introduces three more free parameters (N_{pl} , α , and ν_c), however, within the implementation used by C12, N_{pl} and ν_c are tied to the normalization of the modified blackbody component and dust temperature to produce

⁴ We have tested the effect of allowing β to be a free parameter by re-fitting sources which were detected in all wavebands. We find a median $\beta = 1.8 \pm$, consistent with our choice to fix $\beta = 2.0$. Further we find that all of the derived parameters, especially the integrated luminosities, are consistent within measurement uncertainty with their values when β is fixed at 2.0.

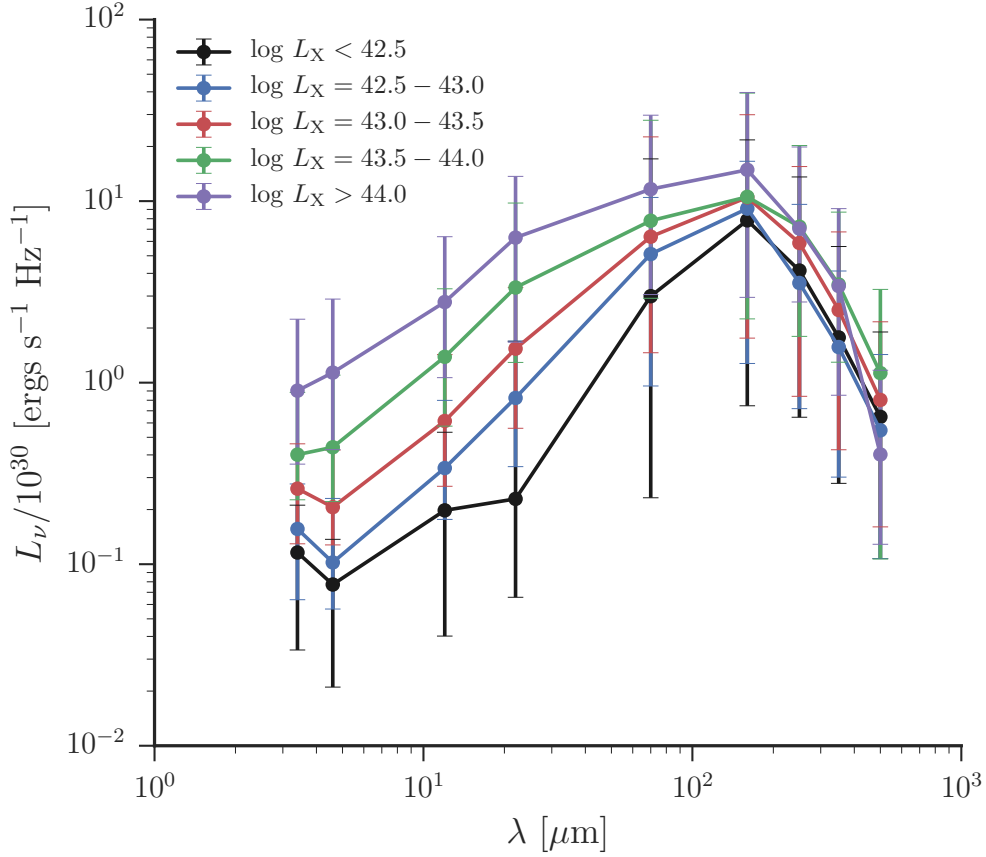


Figure 2. Median IR SEDs in units of 10^{30} ergs s $^{-1}$ Hz $^{-1}$ for the *Herschel*-BAT AGN binned by $L_{14-195\text{keV}}$. Each point in the SEDs is the median L_ν for the whole sample including upper limits calculated using the Kaplan-Meier product-limit estimator. The error bars represent the 68% confidence interval determined from the 16th and 84th percentiles.

Table 1. Best Fit C12 Model Parameters, Luminosities, and AGN Fractions

Name	$\log M_{\text{dust}}$ [M_\odot]	T_{dust} [K]	α	λ_c [μm]	$\log L_{\text{IR}}$ [L_\odot]	$\log L_{\text{SF}}$ [L_\odot]	$\log L_{\text{AGN,IR}}$ [L_\odot]	f_{AGN}
1RXSJ044154.5-082639	$6.80^{+0.21}_{-0.14}$	$27.98^{+2.45}_{-4.21}$	$1.70^{+0.46}_{-0.34}$	$47.71^{+18.85}_{-13.96}$	$10.37^{+0.03}_{-0.04}$	$9.99^{+0.11}_{-0.23}$	$9.99^{+0.11}_{-0.23}$	$0.58^{+0.18}_{-0.14}$
1RXSJ045205.0+493248	$7.47^{+0.12}_{-0.10}$	$23.27^{+0.99}_{-1.91}$	$1.44^{+0.59}_{-0.40}$	$39.95^{+14.82}_{-13.09}$	$10.48^{+0.03}_{-0.03}$	$10.19^{+0.04}_{-0.07}$	$10.19^{+0.04}_{-0.07}$	$0.50^{+0.10}_{-0.10}$
2E1739.1-1210	$7.55^{+0.22}_{-0.19}$	$25.11^{+1.91}_{-3.00}$	$1.46^{+0.51}_{-0.37}$	$45.22^{+16.42}_{-14.16}$	$10.83^{+0.03}_{-0.04}$	$10.46^{+0.07}_{-0.14}$	$10.46^{+0.07}_{-0.14}$	$0.58^{+0.12}_{-0.11}$
2MASSJ07594181-3843560	< 6.58	...	$1.08^{+0.31}_{-0.46}$	$39.20^{+7.93}_{-5.56}$	< 10.63	< 9.63	> 10.59	> 0.90
2MASSJ17485512-3254521	< 6.14	...	$1.45^{+0.56}_{-0.47}$	$44.52^{+18.07}_{-16.37}$	< 9.42	< 9.05	> 8.99	> 0.51
2MASXJ00253292+6821442	$6.16^{+0.39}_{-0.18}$	$25.34^{+2.79}_{-5.06}$	$1.46^{+0.53}_{-0.40}$	$45.40^{+16.38}_{-15.93}$	$9.63^{+0.04}_{-0.05}$	$9.11^{+0.10}_{-0.18}$	$9.11^{+0.10}_{-0.18}$	$0.70^{+0.11}_{-0.11}$
2MASXJ01064523+0638015	$6.81^{+0.69}_{-0.44}$	$21.56^{+9.09}_{-7.50}$	$1.86^{+0.53}_{-0.42}$	$44.58^{+10.57}_{-9.10}$	$10.47^{+0.04}_{-0.05}$	< 9.95	> 10.24	> 0.66
2MASXJ01073963-1139117	$7.66^{+0.09}_{-0.06}$	$25.52^{+1.27}_{-1.96}$	$2.05^{+0.58}_{-0.49}$	$41.53^{+20.19}_{-10.35}$	$10.87^{+0.03}_{-0.03}$	$10.62^{+0.07}_{-0.10}$	$10.62^{+0.07}_{-0.10}$	$0.44^{+0.13}_{-0.12}$
2MASXJ03305218+0538253	$6.76^{+0.69}_{-0.33}$	$28.20^{+6.57}_{-8.76}$	$2.46^{+0.78}_{-0.61}$	$33.77^{+8.47}_{-9.67}$	$10.81^{+0.06}_{-0.06}$	$9.99^{+0.23}_{-0.28}$	$9.99^{+0.23}_{-0.28}$	$0.85^{+0.10}_{-0.13}$
2MASXJ03342453-1513402	$7.43^{+0.05}_{-0.04}$	$26.61^{+0.61}_{-1.09}$	$1.69^{+0.58}_{-0.44}$	$43.00^{+24.14}_{-16.10}$	$10.59^{+0.03}_{-0.03}$	$10.51^{+0.03}_{-0.05}$	$10.51^{+0.03}_{-0.05}$	$0.18^{+0.10}_{-0.10}$

Notes – *Column 1:* Name of the source. *Column 2:* Log of the dust mass in solar units. *Column 3:* Dust temperature for the MBB component. ‘...’ indicates the dust temperature was fixed at 23 K. *Column 4:* Slope of the powerlaw component. *Column 5:* Turnover wavelength. *Column 6:* Log of the total infrared luminosity from 8–1000 μm in solar units. *Column 7:* Log of the MBB component luminosity in solar units. *Column 8:* Log of the powerlaw component luminosity in solar units. *Column 9:* Fractional contribution of the AGN to the total infrared luminosity calculated using Equations 4 and 5. The full version of this table is available in the online publication.

a smoothly varying SED and reduce the number of free parameters from five to three.

But, after early tests using this initial setup, we found that fixing N_{PL} and ν_c as a function of the other parameters produced unreliable fits. This is because AGN SEDs

from the MIR to FIR are not as smooth as those seen in (U)LIRGS, likely due to the disconnect between star-formation and AGN heating. Within starbursting galaxies both the hot and cold dust are related through the same heating process, i.e. star formation, while much of the MIR

emission in AGN host galaxies originates from dust around the AGN with no strong connection to global star formation in the galaxy. Therefore, we chose to leave both N_{PL} and v_c as free parameters resulting in a total of five for the entire model.

We describe in detail within Appendix A the exact fitting method used to estimate each parameter. In short we use a Bayesian framework with a Monte Carlo Markov Chain (MCMC) to probe the posterior probability distribution function (PDF). We marginalize the resulting posterior PDF for each parameter and use the median as our best-fit value and the 16th and 84th percentiles to define our lower and upper uncertainties, respectively.

For the 35 sources with less than four detected points, the parameters of the MBB component are unconstrained. These sources are undetected for several reasons. Either they are a.) intrinsically faint, b.) at relatively large distances, or c.) located in a region with high foreground cirrus emission. This last reason causes problems because it produces high upper limits on the fluxes for the SPIRE wavebands which give the appearance that a substantial amount of FIR emission could exist. Therefore, we tested our modeling with three fixed dust temperatures: 15, 23, and 40 K. 15 and 40 K are the extreme low and high temperatures we find for the whole sample, while 23 K is the median dust temperature. We fit only the 70 – 500 μm points/upper limits and let the dust mass increase until the model SED exceeded one of the points/upper limits.

We find that using a dust temperature of either 23 or 40 K produces consistent MBB luminosities. Using a 15 K dust temperature produces MBB luminosities *lower* than the 23 K and 40 K ones. Therefore its reasonable to assume conservative upper limits on the MBB luminosity can be constrained with a higher dust temperature. The parameter most affected by the choice of temperature is the dust mass. Lower temperatures produce higher upper limits on the dust mass. In fact moving from a 15 K temperature to a 40 K temperature changes the dust mass by two orders of magnitude. Given these tests we choose to run our modeling by fixing the dust temperature at 23 K, the median temperature of our whole sample. We acknowledge that for some of the undetected sources, we might be underestimating the upper limit on the dust mass. Since this subsample is only ~ 10 per cent of the whole, we do not anticipate any large effect on the overall results.

We fit all 313 of the *Herschel*-BAT AGN using the C12 model and report the best fitting parameters in Table 1. Best-fit model SEDs are shown along with the observed SEDs in Figure D1. We also fit HRS galaxies using the exact same model so we can accurately compare the star-forming properties between non-AGN and AGN host galaxies. For the HRS sources with less than four detected points we fix the dust temperature at 21 K, the median dust temperature for the whole HRS sample.

6.2 Luminosities and AGN Fractions

In addition to the parameters associated with the model, we also calculated several luminosities and an AGN fraction. For this work, we define three luminosities: 1) L_{IR} will represent the total infrared luminosity determined by integrating the full SED from 8–1000 μm . 2) L_{SF} will represent

the 8–1000 μm luminosity due to star formation in the host galaxy. 3) $L_{\text{AGN,IR}}$ will represent the 8–1000 μm luminosity due to AGN-heated dust.

L_{IR} for each source was calculated by integrating the best fit model SED from 8–1000 μm . To determine L_{SF} and $L_{\text{AGN,IR}}$ we first start with L_{PL} and L_{MBB} , the 8–1000 μm luminosities of the separate PL and MBB components from our SED decomposition. If we made the assumption that the PL component is completely dominated by the AGN in all sources then we could simply represent L_{PL} as the $L_{\text{AGN,IR}}$ and L_{MBB} as L_{SF} . However, we quickly recognized the PL component for some AGN host galaxies can have a strong contribution from dust heated by stars. Therefore a correction factor must be applied to convert L_{PL} and L_{MBB} into $L_{\text{AGN,IR}}$ and L_{SF} .

We make this correction using the results of the C12 modeling for the HRS sample. Since all of the galaxies in this sample has either no or low-luminosity AGN, the MIR emission is primarily the result of stochastically heated grains near star-forming regions. In Figure 3, we show the distribution of $L_{\text{MBB}}/L_{\text{PL}}$, the ratio of the MBB component luminosity to the MIR powerlaw component. The ratio for the HRS sample is narrowly distributed around a single value, indicating that for our lower mass non-AGN comparison sample the energy contained in the PL and MBB components are tightly connected. We find a median $\log(L_{\text{MBB}}/L_{\text{PL}}) = 0.48 \pm 0.13$, which transforms to $L_{\text{PL,SF}} \approx \frac{1}{3}L_{\text{MBB}}$ where we now indicate the contribution to the PL component from star formation as $L_{\text{PL,SF}}$. We can calculate the AGN contribution for the *Herschel*-BAT AGN then by assuming the star-forming emission follows the same ratio.

$$L_{\text{AGN,IR}} = L_{\text{PL}} - L_{\text{PL,SF}} = L_{\text{PL}} - \frac{1}{3}L_{\text{MBB}} \quad (4)$$

$$f_{\text{AGN}} = L_{\text{AGN,IR}}/L_{\text{IR}} \quad (5)$$

$$L_{\text{SF}} = L_{\text{MBB}} + L_{\text{PL,SF}} = \frac{4}{3}L_{\text{MBB}} \quad (6)$$

The uncertainty on the correction factor leads to an uncertainty on f_{AGN} using this method which we estimate by measuring f_{AGN} for the HRS sample. Figure 4 shows the distribution of “ f_{AGN} ” for HRS. As expected the distribution is centered around 0. We estimate the spread of the distribution by calculating the standard deviation, finding an uncertainty of 0.1. Therefore we add in quadrature an uncertainty of 0.1 to all of our f_{AGN} estimates. Further, any f_{AGN} below 0.1 are converted to upper limits with a value of 0.1.

In Appendix B, we detail our comparison between our chosen C12 model and two other template-based models that aim to decompose the IR SEDs of AGN host galaxies. We find broad agreement between all three models in the measurement of these three luminosities and the AGN fraction. This comparison also provided additional systematic uncertainties on these parameters that we apply for the rest of this work. Further in Appendix C, we analyze the relationship between our measured L_{SF} and polycyclic aromatic hydrocarbon luminosities from *Spitzer*/IRS spectra and compare the relationship with a star-forming galaxy sample. We determine that the relationship between our measured L_{SF} and PAH luminosities is consistent with that seen in a purely star-forming sample.

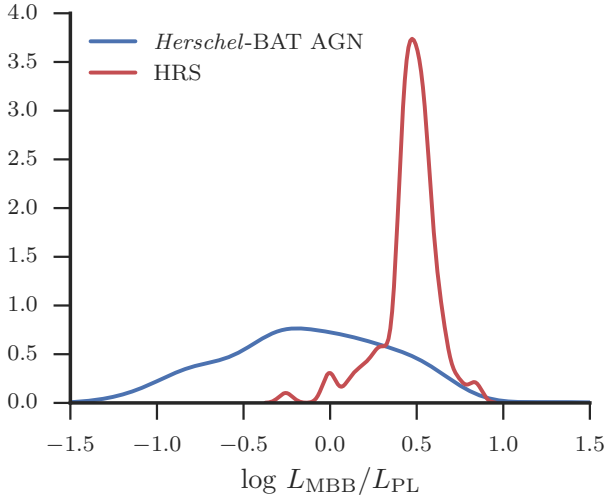


Figure 3. Histograms and Kernel Density Estimates (KDE) of the $L_{\text{MBB}}/L_{\text{PL}}$ distribution for the *Herschel*-BAT AGN (blue), and HRS (red) samples. The HRS galaxies have a narrowly distributed ratio whereas the BAT AGN span a wide range due to the AGN contribution. A color version of this figure is available in the online publication.

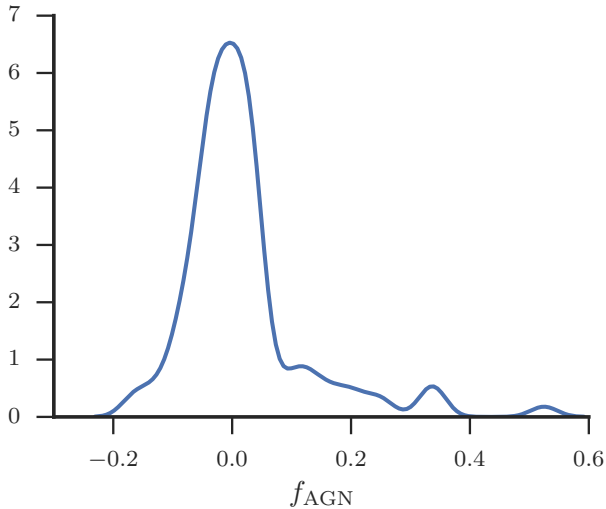


Figure 4. f_{AGN} distribution for HRS. The standard deviation of this distribution quantifies the uncertainty on f_{AGN} associated with the correction factor used to calculate f_{AGN} . A color version of this figure is available in the online publication.

7 RESULTS AND DISCUSSION

7.1 Correlation between $L_{\text{AGN,IR}}$ and $L_{14-195\text{keV}}$

In Figure 5, we plot the relationship between the 14–195 keV luminosity and $L_{\text{AGN,IR}}$. As expected, we find a strong correlation between the two luminosities indicating we have measured $L_{\text{AGN,IR}}$ accurately from the C12 model and our correction factor. To quantify the relationship, we performed linear regression using a PYTHON implementation of LIN-

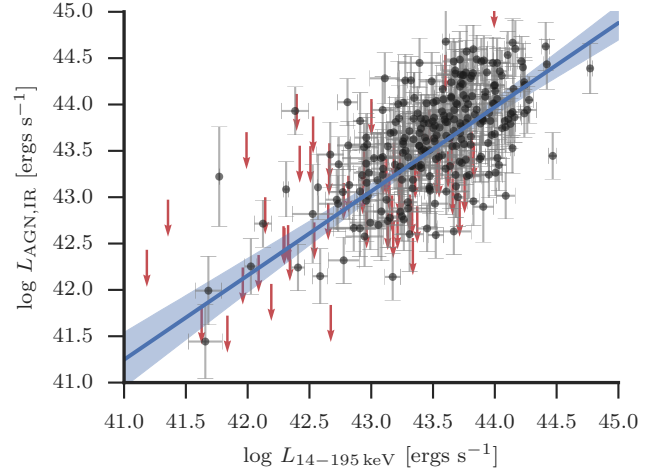


Figure 5. Correlation between $L_{\text{AGN,IR}}$ and $L_{14-195\text{keV}}$ for the *Herschel*-BAT sample (blue points). The solid black line shows the result of Bayesian linear regression with the grey shaded region indicating the 95 per cent confidence interval. The strong correlation between the two luminosities provides evidence our SED decomposition performed well in measuring the IR luminosity associated with AGN heated dust.



MIX_ERR⁵ (Kelly 2007), a Bayesian method for linear regression that incorporates errors in both independent and dependent variables as well as non-detections. Kelly (2007) showed through simulations that LINMIX_ERR outperforms other popular linear regression methods such as ordinary least squares and FIT_EXY. LINMIX_ERR outputs marginalized posterior probability distributions for the slope, intercept, and intrinsic scatter between the two variables as well as the correlation coefficient, ρ . Our reported best fit parameters here and throughout the rest of the Paper will be the median of the marginalized posterior probability distribution with an uncertainty equal to the standard deviation. The linear model assumed is of the form:

$$Y = mX + b + \epsilon_{\text{int}} \quad (7)$$

where Y and X are the dependent and independent variables, m is the slope, b is intercept, and ϵ_{int} represents intrinsic scatter in the relationship beyond that related to measurement error. ϵ_{int} is modeled as a Gaussian random variable with mean 0 and a variance of σ^2 .

We plot the best fit linear regression for the whole sample in Figure 5 as a black line with grey shading to indicate the 95 per cent confidence interval. The best-fit line corresponds to the following relationship:

$$\log(L_{\text{AGN,IR}}) = (0.91 \pm 0.06) \log(L_{14-195\text{keV}}) - (4.03 \pm 2.6) \quad (8)$$

The correlation coefficient from LINMIX_ERR is 0.8 ± 0.03 and the intrinsic scatter is 0.15 dex. Our measured slope of 0.90 is slightly flatter than the slope measured in Gandhi

⁵ <https://github.com/jmeyers314/linmix>

et al. (2009) ($m = 1.1$) using sub-arcsecond $12\ \mu\text{m}$ imaging for 16 nearby Seyferts. However, given our very simple method for determining the AGN MIR luminosity from broadband SED decomposition, a slope close to 1.0 and high correlation coefficient provides confidence that the decomposition has performed reasonably well. Further, Equation 8 will provide future studies with estimates of the full 8–1000 μm AGN contribution and allow better estimates of IR-based SFRs for AGN as long X-ray data is available.

Because we are comparing luminosities and the *Swift*/BAT sample if flux-limited, the correlation we see could simply be due to a confounding variable, in this case distance. To investigate this possibility, we performed a partial correlation test with ASURV using distance as our third variable along with the 14–195 keV luminosity and AGN-related IR luminosity. The partial correlation test calculates Kendall’s- τ rank correlation coefficient between all three variables, then estimates the intrinsic correlation coefficient after removing the dependence on the third variable (i.e. distance).

We find $\tau = 0.30 \pm 0.03$ and reject the null hypothesis of zero partial correlation at a significance level of 10^{-23} . While the value of the correlation coefficient is less than the correlation coefficient from LINMIX_ERR, the partial correlation test does not account scatter due to measurement error.

7.2 IR colors as a predictor of f_{AGN} and selecting AGN

We utilize our broad coverage of the IR SED for AGN host galaxies to test the viability of different IR colors for predicting the AGN IR luminosity fraction (i.e. f_{AGN}). For large surveys and/or high redshift studies, coverage from 12–500 μm might not be available or possible.

In Figure 6, we plot six MIR/FIR flux ratios (12/70, 12/160, 12/250, 22/70, 22/160, 22/250) against the measured f_{AGN} for the *Herschel*-BAT AGN. The flux ratios are all in log units to better visualize the relationships. Upper limits on f_{AGN} are shown as downward-pointing arrows. In the lower right corner of each subplot, we show representative error bars. We fit a linear model between each flux ratio and f_{AGN} with the following form

$$f_{\text{AGN}} = m \log(F_1/F_2) + b + \epsilon_{\text{int}} \quad (9)$$

where F_1/F_2 represents each flux ratio. To calculate the best fitting parameters, we again used LINMIX_ERR.

Table 2 outlines the best fit parameters for each relationship. Each flux ratio is highly correlated with f_{AGN} (all $\rho > 0.87$). It is clear however that the worst indicators are the flux ratios involving the 250 μm flux with ρ less than 0.9 as well as showing significant scatter in Figure 6.

Based on the slope of the linear regressions, the 22/70 μm , with a slope of 0.8, overall seems to be the best flux ratio to use as an indicator of the AGN contribution to the IR SED. These two wavebands bracket the region where the intrinsic AGN SED is thought to turnover Netzer et al. (e.g. 2007); Mullaney et al. (e.g. 2011) and seems to be the crucial transition region where the SED shifts from AGN-dominated to host galaxy dominated.

We further test how well each IR color exclusively selects AGN host galaxies. In Figure 6 we plot the 75th, 50th,

and 25th percentile color for the *Herschel*-BAT sample as blue dashed (for the 25th and 75th percentiles) and blue solid (for the 50th percentile) vertical lines. In Table 2, the last three columns list the colors in logarithmic units for the 75th, 50th, and 25th percentiles. These colors mean that by selecting galaxies with a color above this one, the sample will be 75, 50, and 25 per cent complete based on the *Herschel*-BAT sample.

While these colors are useful for selecting AGN host galaxies, we also want to know what percentage of non-AGN galaxies would be selected with these color cuts as contamination for a sample. Therefore, we also calculated the percentile of HRS galaxies that would be selected. For this analysis, we used the complete HRS sample since it represents the natural field galaxy population and we do not want to restrict to only high-mass non-AGN galaxies. The HRS sample unfortunately was not observed at 70 μm , therefore to calculate the 12/70, and 22/70 colors, we simply used the 70 micron flux from the best-fit model. The percentiles for HRS are given in parentheses next to the values of the colors in Table 2.

We find that the best color to use in selecting an AGN-only sample would be the 22/160 color. Using the 75th percentile color (-1.14), we would only select 5.6 per cent of the HRS sample. To get only around 1 per cent of the HRS sample, we would have to use the 50th percentile 22/160 or 22/250 color, however this would only select half of a complete AGN sample. To select no non-AGN galaxies would require pushing to the 25th percentile colors and risk severe incompleteness and a selection bias of only AGN-dominated galaxies. In a forthcoming paper, we will evaluate these colors along with other MIR color selection techniques (e.g. Donley et al. 2012; Stern et al. 2012) to determine the biases and selection effects with regards to the SFR of the galaxy and strength of the AGN.

7.3 The AGN contribution to the 70 μm emission

Many studies examining the relationship between nuclear activity and star formation rely on single monochromatic luminosities as an indicator of star formation (e.g. Netzer et al. 2007; Netzer 2009; Rosario et al. 2012). The most widely used indicator has been the 60 μm luminosity given its availability from the all-sky *IRAS* survey.

With our *Herschel*-BAT sample and SED modeling we can test how often and at what level AGN emission contributes to different wavelength bands. We test the AGN contribution to the 70 μm emission. Based on visual inspection of all of the SED fits, we found this waveband is the only *Herschel* band with a noticeable AGN contribution. All other longer wavelength bands were dominated by the MBB component. We restrict this analysis to only those sources with well-determined SEDs longwards of 70 μm , excluding those objects with less than four detected SED points. We note that the majority of these objects are likely AGN dominated at 70 μm , however the uncertainty in their FIR SED, especially their dust temperature results in a largely unconstrained calculation.

To determine the AGN contribution to the 70 μm emission, we first estimated the PL component associated with star formation. We assumed the shape of the star-forming PL component followed the average power law slope ($\alpha = 0.0$

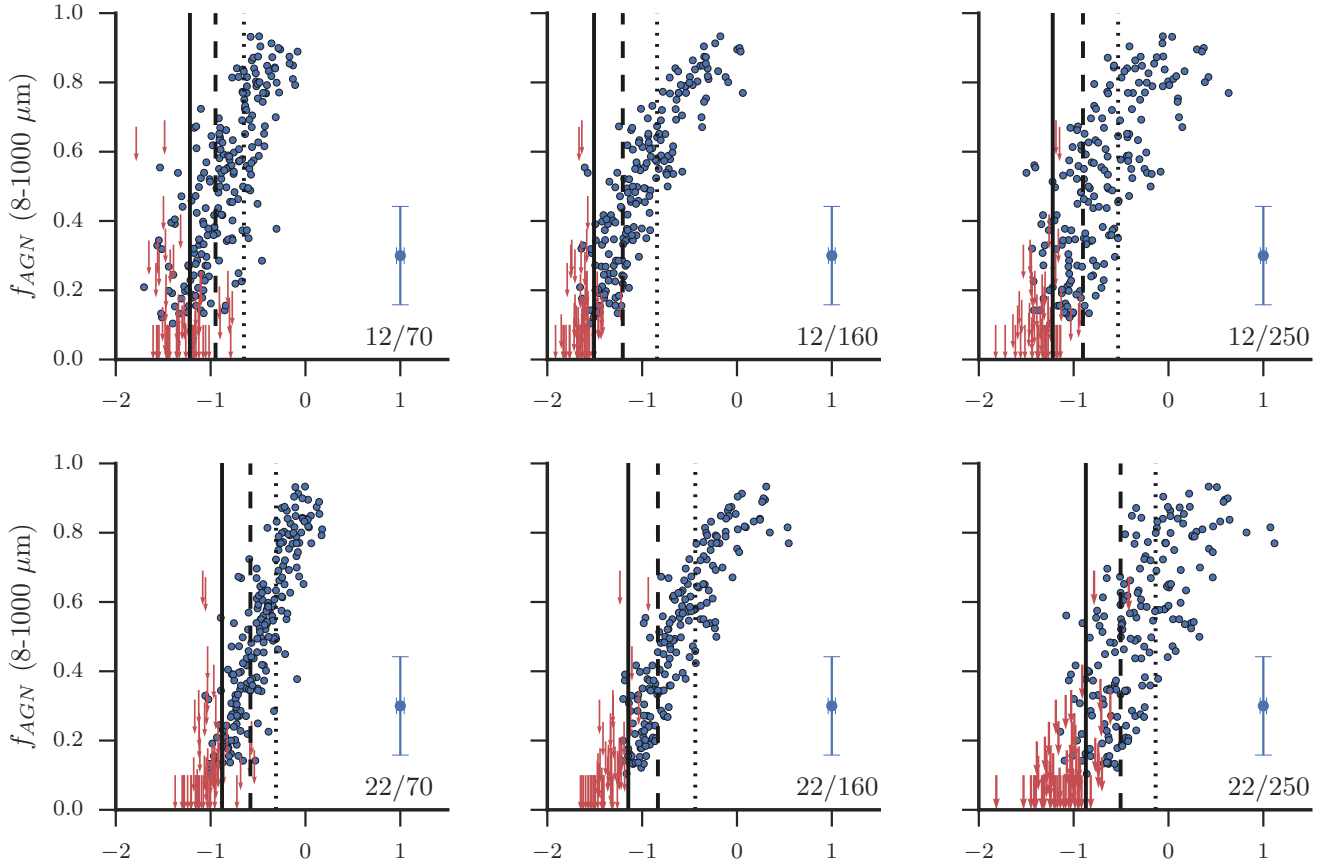


Figure 6. Relationship between different IR colors and the f_{AGN} , the fraction of the 8–1000 μm luminosity attributed to AGN heated dust. The IR colors (x-axis) are in logarithmic units. Upper limits on f_{AGN} are indicated as red arrows and are at 95% confidence. We also display the 75th, 50th, and 25th percentile colors for the *Herschel*-BAT AGN as solid, dashed, and dotted vertical lines, respectively. Choosing a sample with colors *above* these would result in 75, 50, and 25 per cent completeness for the *Herschel*-BAT AGN.

Table 2. Linear Regression Between Flux Ratios and f_{AGN}

F_1/F_2	m	b	σ_{int}	ρ	75th %tile (%tile for HRS)	50th %tile (%tile for HRS)	25th %tile (%tile for HRS)
12/70	0.67 ± 0.04	1.02 ± 0.03	0.016 ± 0.004	0.89 ± 0.02	-1.23 (90)	-0.97 (50)	-0.66 (21)
12/160	0.58 ± 0.02	1.05 ± 0.03	0.002 ± 0.002	0.99 ± 0.01	-1.51 (31)	-1.21 (5.2)	-0.85 (2.2)
12/250	0.51 ± 0.03	0.84 ± 0.03	0.019 ± 0.004	0.87 ± 0.03	-1.22 (28)	-0.91 (5.2)	-0.57 (1.5)
22/70	0.79 ± 0.03	0.86 ± 0.02	0.001 ± 0.001	0.99 ± 0.01	-0.89 (32)	-0.60 (16)	-0.32 (12)
22/160	0.58 ± 0.02	0.85 ± 0.02	0.0004 ± 0.0005	0.997 ± 0.003	-1.14 (5.6)	0.83 (1.2)	-0.45 (0)
22/250	0.49 ± 0.03	0.65 ± 0.02	0.016 ± 0.004	0.90 ± 0.02	0.87 (6.8)	-0.51 (0.02)	-0.18 (0)

and turnover wavelength ($\lambda_c = 50 \mu\text{m}$) from the HRS sample. We then adjusted the normalization such that the integrated luminosity would equal $1/3 L_{\text{MBB}}$. We combined the estimated star forming PL component with the measured MBB component to form each of the *Herschel*-BAT AGN's total star-forming component. The 70 μm AGN contribution was then calculated as the excess 70 μm emission leftover after subtracting the star-forming contribution from the total 70 μm emission from the best-fit SED. We denote the fraction contributed by the AGN as $f_{\text{AGN},70}$.

Figure 7, *left* shows the distribution of $f_{\text{AGN},70}$. We find that for 48 per cent of the sample, $f_{\text{AGN},70} < 0.2$ but for 24 per cent of the sample $f_{\text{AGN},70} > 0.5$. Using the 70 μm lumi-

osity as a single SFR indicator would overestimate values by at least a factor of 2 for almost one-third of an AGN sample.

In the right panel of Figure 7 we show $f_{\text{AGN},70}$ as a function of the 14–195 keV luminosity. The grey points indicate the individual points while the blue points with error bars are binned averages with a 68 per cent confidence interval determined through bootstrapping. It is abundantly clear that at $\log L_{14-195 \text{ keV}} < 42.5$, $f_{\text{AGN},70}$ is largely negligible with only two sources with $f_{\text{AGN},70} > 0.2$. These AGN are NGC 1052 and NGC 4941. Both are quite pointlike, possibly unresolved at 70 μm , while at long wavelengths show large-scale extended emission.

Above $\log L_{14-195\text{ keV}} = 42.5$, the AGN contribution at $70\text{ }\mu\text{m}$ varies nearly uniformly between 0 and 1. This indicates that the AGN contribution is not a simple function of high AGN luminosity, rather it is due to the competing interplay between AGN emission and star-formation. This reinforces the need for SED decomposition to determine accurate SFRs when an AGN is present. We did repeat this process at $160\text{ }\mu\text{m}$, finding no source indicated an AGN contribution above the 5 per cent level.

7.4 M_{dust} , T_{dust} , and SFR of local AGN host galaxies

Figure 8 compares the distribution of M_{dust} , T_{dust} , and SFR for our three samples of galaxies. We calculated SFRs using the conversion from 8–1000 μm star-forming luminosity using the following equation from Murphy et al. (2011)

$$\text{SFR} = \frac{L_{\text{SF}}}{2.57 \times 10^{43}} \quad (10)$$

The solid lines show the KDE for sources which have firm measurements while the dashed lines show the KDE for the sources with only upper limits. Table 3 displays the median for these three properties and each sample. The values inside parentheses indicate the 16th and 84th percentiles for each distribution. The median, 16th, and 84th percentiles were calculated using survival analysis and the KMPL as in Section 5 to account for upper limits.

We find that the *Herschel*-BAT AGN have higher dust masses than the HRS sample, slightly higher dust temperatures, and higher SFRs. Because we have mass-matched the HRS sample to the *Herschel*-BAT sample, there should be no effects due to stellar mass. To confirm that the distributions are statistically different we run the Peto-Prentice two-sample test. The Peto-Prentice two sample test is comparable to the Kolmogorov-Smirnov (K-S) test which calculates the probability that two separate samples were drawn from the same parent population. The Peto-Prentice test, however, allows for the inclusion of censored data.

For the comparison of dust masses, we find the probability that the *Herschel*-BAT AGN and HRS galaxies are drawn from the same parent distribution is 1.8×10^{-5} . The probability for the dust temperatures is 4×10^{-4} , while the probability for the SFRs is 8.4×10^{-11} . All three probabilities are less than 0.05, the standard cutoff for declaring two samples are inconsistent with being drawn from the same parent population.

The increased SFRs for the *Herschel*-BAT sample compared to the mass-selected HRS sample are consistent with the results of Koss et al. (2011). Koss et al. (2011), using optical colors, found that the *Swift*/BAT AGN displayed bluer colors compared to a mass-matched sample of Sloan Digital Sky Survey (SDSS) galaxies, indicative of increased levels of star formation.

These results may seem contradictory with our previous work in Shimizu et al. (2015) where we detail using the SFRs calculated here that AGN host galaxies are experiencing decreased levels of star formation given their stellar mass. However, the discrepancy lies in the comparison being done. In Shimizu et al. (2015) we compare the *Herschel*-BAT AGN to the so-called star-forming “main sequence,” a tight nearly

linear correlation between SFR and M_{star} (Brinchmann et al. 2004; Salim et al. 2007; Noeske et al. 2007), finding the AGN are falling off and transitioning towards quiescence. In this work as well as in Koss et al. (2011), simple mass-matching is used to form comparison samples which leads to selecting only high stellar mass non-AGN galaxies due to the high stellar masses of the BAT AGN. Based on previous studies of the color-magnitude relation, however, selection of high mass galaxies will result in a large quiescence fraction (Kauffmann et al. 2003; Wuyts et al. 2011) especially at low redshifts (Bell et al. 2012). Therefore, since the *Herschel*-BAT AGN show both intermediate optical colors and SFRs, it makes sense that a mass-selected non-AGN sample with indicate bluer colors and higher SFRs for AGN host galaxies given quiescent galaxies are largely red with low SFRs.

Further, looking into the details of our mass-selected HRS sample, we find that 47/122 (50%) are morphologically classified as early type (E/S0), the dominant morphology for quiescent galaxies (Wuyts et al. 2011; Bell et al. 2012). The *Herschel*-BAT AGN, though, are largely late type spirals Koss et al. (2011) and even the few ellipticals in our sample show higher SFRs than expected for quiescent galaxies (Shimizu et al. 2015). Thus, it seems clear that we can reconcile the results of Koss et al. (2011), Shimizu et al. (2015), and this work by understanding that mass-matching preferentially selects low star-forming, red galaxies in contrast to the intermediate star-forming, blue AGN.

The higher SFRs immediately explain slightly larger dust masses observed for the *Herschel*-BAT AGN.⁶ The *Herschel*-BAT AGN have a median $\log M_{\text{dust}}$ of 7.38 M_{\odot} vs. 7.0 M_{\odot} for the HRS. The 16th percentiles also extend to much lower dust masses for the HRS. Cortese et al. (2012a) showed using the full HRS sample that the dust-to-stellar mass ratio is anti-correlated with $NUV-r$ color, a proxy for specific SFR and decreases strongly when moving from late type to early type galaxies. da Cunha et al. (2010) also showed, using over 3000 galaxies from SDSS, a strong correlation between the cold dust mass of galaxies and their SFR.

The increased dust temperatures observed in the *Herschel*-BAT AGN could also be explained by the increased SFRs. Dust temperatures are known to increase with both infrared luminosity and specific SFR (e.g Chapman et al. 2003; Symeonidis et al. 2013; Cortese et al. 2014; Magnelli et al. 2014), although both of those studies did not extend to the low luminosities and specific SFR we observe in our samples. Because we know our sample contains an AGN, it is possible at least some of the increased dust temperatures could be to AGN heating. Recently, García-González et al. (2016) spatially decomposed the FIR images of a small sample of nearby Seyfert galaxies and found that nuclear emission shows markedly higher dust temperatures than the host galaxy (as probed through the 70/160 μm color). Sources that are dominated by nuclear emission should then show higher temperatures that do not match with the overall correlation between SFR and T_{dust} .

In Figure 9, we show the relationship between SFR

⁶ Excluding the objects with only upper limits on the dust mass, which are dependent on the assumed fixed dust temperature we used in the modeling (see Section 6 produces the same overall trend of higher dust masses in the *Herschel*-BAT AGN sample

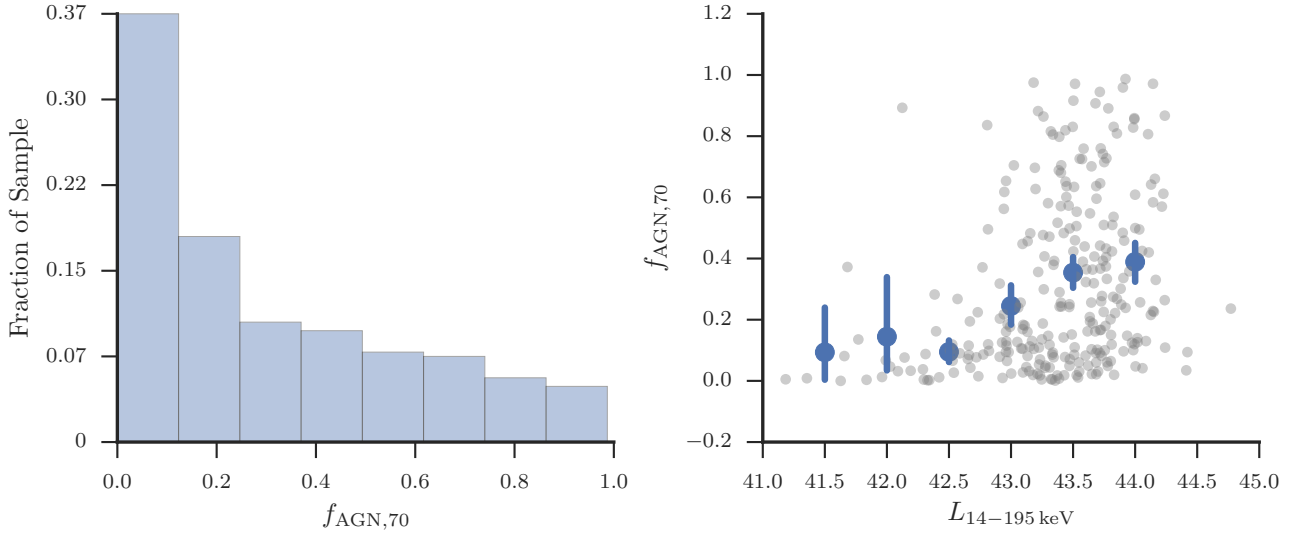


Figure 7. *left:* Histogram of the estimated $70\ \mu\text{m}$ contribution by AGN-heated dust. Each bar is a bin with a width of 0.1 and a height equal to the fraction of the total sample. *right:* Relationship between the 14–195 keV luminosity and $70\ \mu\text{m}$ AGN contribution. Grey dots represent each individual source while the blue dots with error bars are averages within bins according to 14–195 keV luminosity. Error bars indicate the 68 percent confidence interval determined using bootstrap analysis.

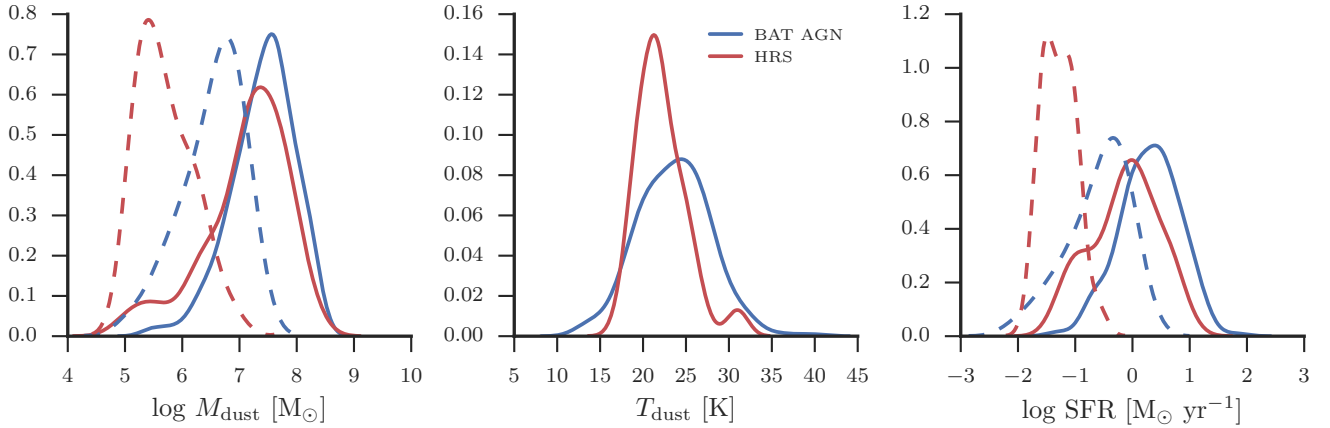


Figure 8. Comparison of M_{dust} , T_{dust} , and SFR between the *Herschel*-BAT AGN (blue), and HRS mass-matched sample (red). The distributions with dashed lines indicate sources with only upper limits on these values. A color version of this figure is available in the online publication.

Table 3. Mean M_{dust} , T_{dust} , and SFR

Sample	$\log M_{\text{dust}}$ [M_{\odot}]	T_{dust} [K]	$\log \text{SFR}$ [$M_{\odot}\ \text{yr}^{-1}$]
<i>Herschel</i> -BAT	7.36 (6.56–7.90)	23.8 (19.4–27.5)	0.23 (−0.57–0.81)
HRS	7.08 (5.12–7.70)	21.5 (19.4–24.6)	−0.23 (−1.57–0.36)

and T_{dust} for the *Herschel*-BAT AGN and HRS galaxies. The bulk of both samples follow in general a broad positive correlation. There exists a group of HRS galaxies at low SFR ($\log \text{SFR} < -1.0$) that show a flat relationship with T_{dust} . All but one of these galaxies are early type which are known to show dust temperatures up to 30 K (Temi et al. 2007). The encircled *Herschel*-BAT AGN at $T_{\text{dust}} > 30$

K and $\log \text{SFR} < 0.5$ seem to represent distinct outliers from both samples. These sources are 2MASX J09235371-3141305, 2MASXJ 15462424+6929102, ESO 103-035, ESO 417-G006, MCG −05-23-016, MCG −06-30-015, Mrk 841, and NGC 3516. Except for 2MASX J09235371-3141305, these sources also all have $f_{\text{AGN}} > 0.5$, indicating the MIR PL component is quite dominant. ESO 103-035, MCG −05-23-016,

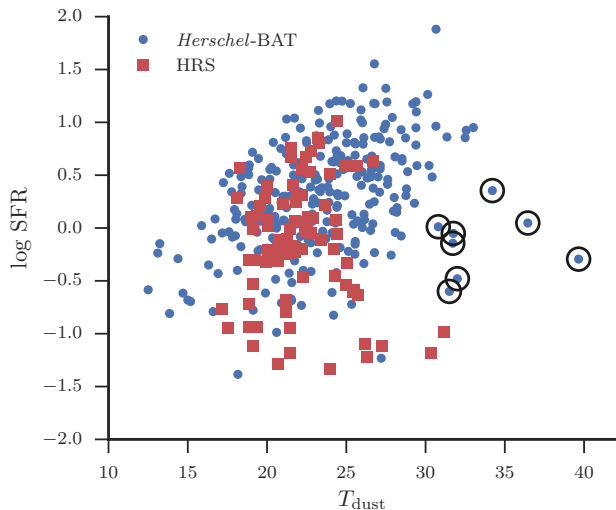


Figure 9. Correlation between dust temperature and SFR for the *Herschel*-BAT AGN (blue points) and HRS galaxies (red squares). Circled blue points indicate possible sources that are dominated by AGN-heated dust.

and Mrk 841 show SEDs that peak around $20\ \mu\text{m}$, highly indicative of an SED dominated by IR emission from the AGN. For these seven AGN, then, it is possible that the large dust temperatures are due to AGN heating, rather than star formation.

Besides the seven sources listed, though, the bulk of the *Herschel*-BAT AGN seem to show T_{dust} largely consistent with star-formation heated dust and coincident with our results for M_{dust} and the SFR.

7.5 The Correlation Between SFR and AGN Luminosity

Our main goal in this Paper is to assess the observational evidence for a connection between AGN and star formation in their host galaxy. To accomplish this, we analyze the correlation between the AGN strength and SFR. We assume the 14–195 keV luminosity ($L_{14-195\text{keV}}$) linearly probes the bolometric AGN luminosity as shown by Winter et al. (2012). L_{SF} measures the SFR using Equation 10.

Figure 10 plots the correlation between the SFR and $L_{14-195\text{keV}}$ for the *Herschel*-BAT AGN. Black points with error bars indicate all of our detected sources, while red arrows show 95 per cent confidence upper limits for objects with less than four SED points. We determine parameters for the following linear model:

$$\log \text{SFR} = m \log L_{14-195\text{keV}} + b + \epsilon_{\text{int}} \quad (11)$$

using LINMIX_ERR as before. The blue line and shaded region in Figure 10 represents the best-fit line and 95 percent confidence interval. We find a best fitting $m = 0.18 \pm 0.07$, $b = -7.85 \pm 2.93$, and $\sigma^2 = 0.37 \pm .04$ with a correlation coefficient of only $0.17 \pm .06$.

Our measured AGN-SFR relationship agrees mainly with the previous studies that found a flat or weak relationship (Silverman et al. 2009; Diamond-Stanic & Rieke

2012; Mullaney et al. 2012; Azadi et al. 2015; Stanley et al. 2015). The scatter in the relationship is high covering nearly 2 orders of magnitude in SFR for a given AGN luminosity. In Figure 11, we compare our correlation with previous measured relationships at low redshift from Rosario et al. (2012) (red dashed line) and Netzer (2009) (black dashed line). The blue points show the median log SFR in bins of 14–195 keV luminosity with error bars indicating the 16th and 84th percentiles.

Our correlation does not agree with either Rosario et al. (2012) or Netzer (2009) showing both a lower normalization, no upturn at high luminosities and a much flatter slope. The slope of the Netzer (2009) relationship is 0.8 which also coincides with the slope of the Rosario et al. (2012) relationship at high luminosities. Both studies, however, used the $60\ \mu\text{m}$ luminosity as a measure of the SFR which we showed in Section 7.3 can be strongly influenced by the AGN. Netzer (2009) also chose to only measure the relationship in AGN-dominated objects leading to an even greater effect of the AGN contribution. At high luminosities, the upturn seen in the Rosario et al. (2012) relationship could be due to Malmquist bias. Even though their sample was based on the *Swift*/BAT AGN, just as ours, no redshift cutoff was applied. Due to the flux-limited nature of the *Swift*/BAT catalogue, there is a strong selection bias where the highest luminosity objects are preferentially at high redshift which will introduce a correlation based on distance rather than an intrinsic one. Rosario et al. (2012) also only used *IRAS* detected sources. The lower sensitivity of *IRAS* compared to *Herschel* can explain the reduced normalization we see. Combined with the work of Azadi et al. (2015) and Stanley et al. (2015), we can firmly say that for all redshifts including the local universe, individual SFRs are not related to the current AGN luminosity.

Two different but not mutually exclusive explanations have been proposed to explain the lack of relationship seen between the strength of the AGN and SFR. Diamond-Stanic & Rieke (2012) suggest that the AGN only influences star formation in the nuclear regions of galaxies and find that when restricting their measurements to only the inner 1 kpc, a stronger relationship appears. Esquej et al. (2014), probing even smaller scales ($r < 100\ \text{pc}$) using MIR interferometry, also found a nearly linear relationship between the nuclear SFR and SMBH accretion rate, and LaMassa et al. (2013), cleverly utilizing the fixed aperture of the SDSS fiber, found that only within 1.7 kpc a positive relationship between the SFR and accretion rate occurs. These are all in agreement with hydrodynamical simulations (Hopkins & Quataert 2010; Thacker et al. 2014) that predict an increasingly linear relationship as the star formation size scale decreases. Work is currently ongoing to spatially decompose the SFRs of the *Herschel*-BAT sample to determine whether the relationship strengthens near the nucleus.

The second explanation involves the varying timescales associated with star formation and accretion onto the SMBH. Measuring the SFR from the IR luminosity results in an average SFR over nearly 100 Myr (Kennicutt & Evans 2012) while the X-ray luminosity is more aligned with the instantaneous AGN luminosity especially given the observations that the X-ray emission likely originates very near to the SMBH (e.g. Chen et al. 2011). Therefore, if the AGN luminosity can vary over 100 Myr, while the SFR is rela-

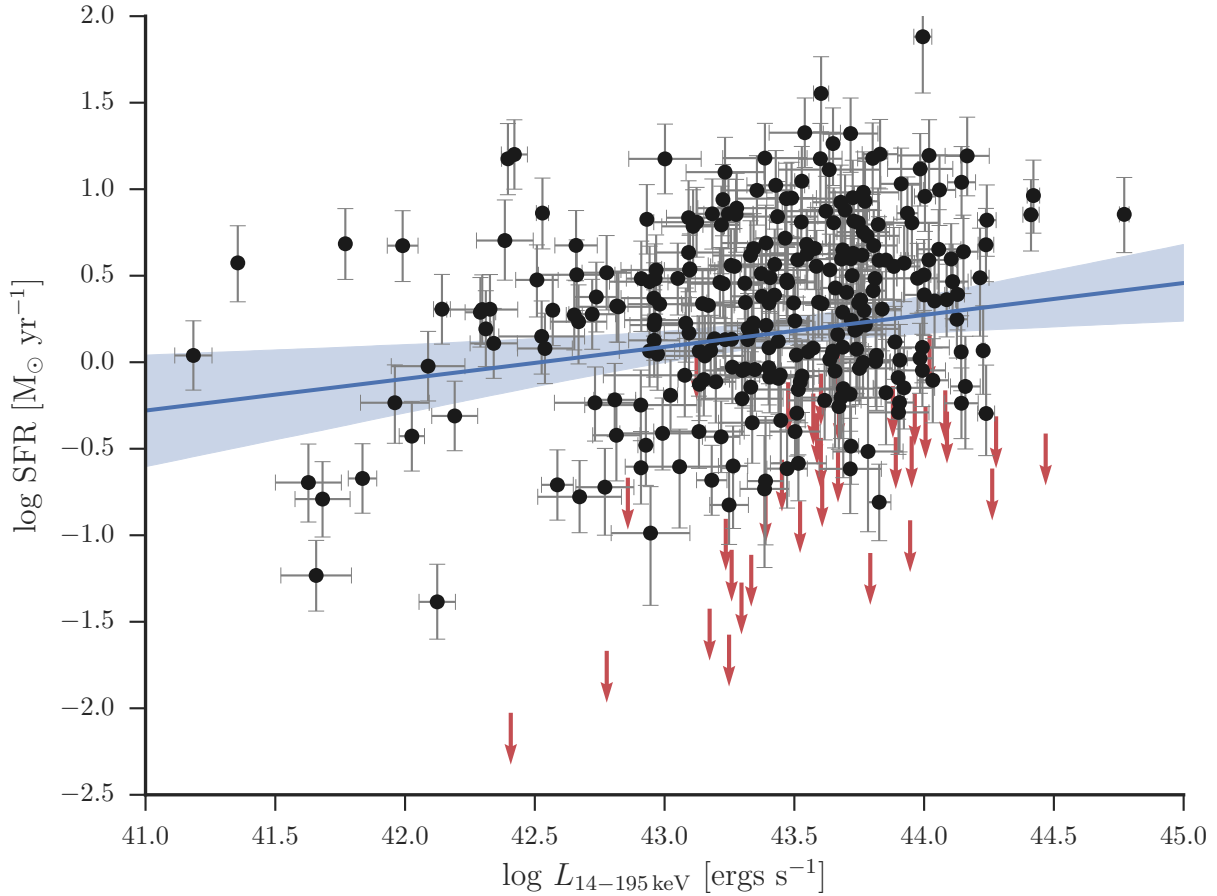


Figure 10. Correlation between AGN luminosity as probed by $L_{14-195\text{keV}}$ and SFR. Error bars on $L_{14-195\text{keV}}$ correspond to the 90 percentile confidence interval from the 58 month BAT catalogue. Error bars on the SFR correspond to the 68 percentile confidence interval from our SED fitting. Downward pointing arrows plot 95 percent confidence upper limits on the SFR. The solid blue line with shading plots the best fit line and 95 percentile confidence interval for our AGN-SFR relationship from LINMIX_ERR. No strong relationship exists between the AGN strength and global star formation. A color version of this figure is available in the online publication.

tively stable, this will cause any intrinsic relationship between the two to weaken. Hickox et al. (2014) explored this using a simple model for the Eddington ratio distribution for an AGN and a linear relationship between the AGN luminosity and SFR, finding that a powerlaw Schechter function matches the observed weak AGN-SFR relationship. However this was based on the upturns seen in the relationships from Rosario et al. (2012) which we clearly do not observe suggesting that adjustments need to be made to conform with our observations.

Neither explanation however needs to invoke AGN feedback. A intrinsically positive correlation between the SFR and AGN luminosity, whether on small spatial scales or long timescales can simply be explained by the availability of their common fuel, namely cold gas. Large amounts of cold gas will spur both high accretion rates and high SFRs. Certainly observations that X-ray detected AGN lie below the star-forming main sequence Shimizu et al. (2015); Mat-suoka et al. (2015); Mullaney et al. (2015) is suggestive that the AGN plays some role in quenching. AGN-driven outflows that are likely suppressing star formation have been observed in small samples (Veilleux et al. 2013; Ciccone et al. 2014; Tombesi et al. 2015); but in a recent study of 50 nearby

Swift/BAT AGN, Stone et al. (2016) found only four objects with evidence for a molecular outflow, strengthening the argument that AGN only contribute to driving gas out of the galaxy at high luminosity ($L_{\text{AGN}} > 10^{45} \text{ ergs s}^{-1}$). Instead its equally possible that at least some of our galaxies are going through passive quenching, whereby gas is simply being slowly depleted through star-formation and star-formation driven outflows after accretion onto the galaxy has slowed or been shut off (Peng et al. 2015). This scenario agrees with the so-called “bathtub” model for galaxy evolution first proposed in Lilly et al. (2013). The fact we observe the majority of AGN host galaxies in transition would simply be a consequence that AGN activity is more likely in gas-rich galaxies (Vito et al. 2014) but there is a delay between the peak of star formation and accretion onto the SMBH (Davies et al. 2007; Schawinski et al. 2014). This is supported by our results that AGN have higher dust masses along with higher SFRs than mass-matched field galaxies, assuming the dust-to-gas ratio is constant.

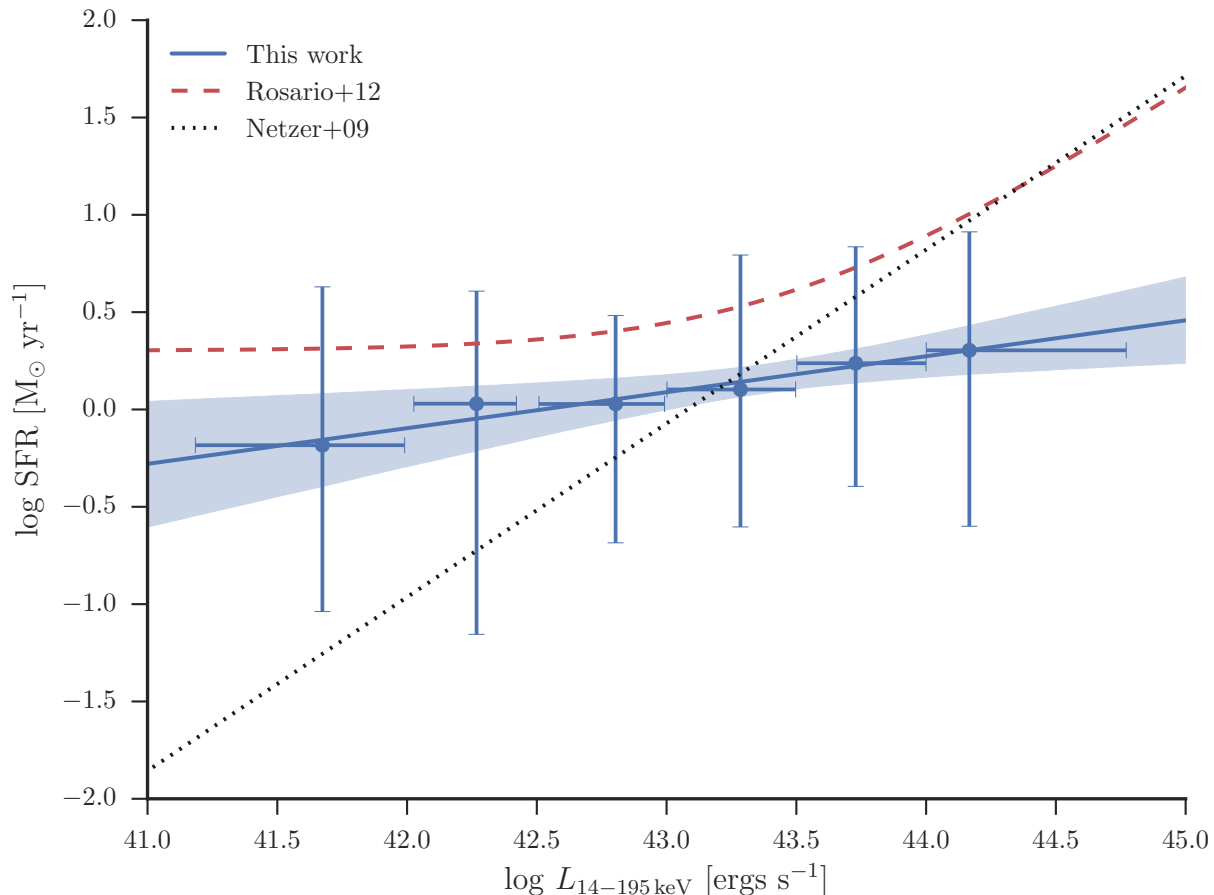


Figure 11. Comparison between the measured SFR- $L_{14-195\text{ keV}}$ from the *Herschel*-BAT sample (blue line with shaded region) and previous relationships from Netzer (2009) (dotted line) and Rosario et al. (2012) (red dashed line). The points with error bars are the median SFRs binned by $L_{14-195\text{ keV}}$ from the *Herschel*-BAT sample. Error bars represent the 68 per cent confidence interval. A color version of this figure is available in the online publication.

8 CONCLUSIONS

Using our high quality *Herschel* photometry from Meléndez et al. (2014) and Shimizu et al. (2016) combined with archival *WISE* 12 and 22 μm photometry, we have constructed and modeled the SEDs for over 300 AGN. Our sample is unique given its nearly unbiased selection based on ultra-hard X-ray detection as well as its local nature that eliminates possible biases and source confusion. The following is a summary of our results and conclusions.

(i) After correcting for host galaxy contribution, we find a nearly linear correlation between the estimated 8–1000 μm luminosity due to the AGN and the 14–195 keV luminosity signifying our decompositions are accurate.

(ii) We determined relationships between various MIR and FIR colors as a proxy for the AGN contribution to the total 8–1000 μm luminosity (f_{AGN}), finding that the 22/70 and 22/160 colors follow the best relationship with f_{AGN} .

(iii) We investigated the AGN contribution to the 70 μm emission of a galaxy and showed that for nearly 30 per cent of our sample, more than half of the 70 μm flux is likely due to AGN heating.

(iv) We calculated a median dust mass of $10^{7.36} M_{\odot}$, dust temperature of ~ 24 K, and SFR of $1.7 M_{\odot} \text{ yr}^{-1}$ for AGN

host galaxies. In a comparison with a mass-matched sample of non-AGN, we find all three properties are systematically higher by a factor 2 for the dust mass, 2 K in dust temperature, and a factor of 3 in SFR. This can be explained as a consequence of high mass non-AGN samples largely being composed of quiescent early type galaxies.

(v) Confident in our measures of the SFR, we find a nearly flat (slope = 0.18 ± 0.07) relationship between the SFR and AGN luminosity, in agreement with previous studies at higher redshift. Our flat relationship is in contrast to previous low redshift studies that find either a nearly linear relationship or an upturn at high luminosities. We suspect this is due to either AGN contamination or Malmquist bias. If nuclear activity is related to global star formation, it is only on long timescales, however another possible explanation is that the relationship strengthens only as the physical scales probed decrease.

It is abundantly clear now that AGN activity is not related to the global SFR as probed by the X-ray luminosity and FIR emission. However we are working to determine whether spatial decomposition combined with our SED decomposition can illuminate the exact nature of the relationship between the AGN and nuclear star formation. This will

also further test our simple decomposition methods and help expand our knowledge of the intrinsic AGN infrared SED into the FIR regime.

ACKNOWLEDGEMENTS

This publication makes use of data products from the Wide-field Infrared Survey Explorer, which is a joint project of the University of California, Los Angeles, and the Jet Propulsion Laboratory/California Institute of Technology, and NEOWISE, which is a project of the Jet Propulsion Laboratory/California Institute of Technology. WISE and NEOWISE are funded by the National Aeronautics and Space Administration.

REFERENCES

- Aird J., et al., 2010, *MNRAS*, **401**, 2531
- Asmus D., Hönig S. F., Gandhi P., Smette A., Duschl W. J., 2012, *Journal of Physics Conference Series*, **372**, 012034
- Azadi M., et al., 2015, *ApJ*, **806**, 187
- Barger A. J., Cowie L. L., Owen F. N., Chen C.-C., Hasinger G., Hsu L.-Y., Li Y., 2015, *ApJ*, **801**, 87
- Baum S. A., et al., 2010, *ApJ*, **710**, 289
- Bell E. F., et al., 2012, *ApJ*, **753**, 167
- Bianchi S., 2013, *A&A*, **552**, A89
- Boselli A., et al., 2010, *PASP*, **122**, 261
- Bower R. G., Benson A. J., Malbon R., Helly J. C., Frenk C. S., Baugh C. M., Cole S., Lacey C. G., 2006, *MNRAS*, **370**, 645
- Boyle B. J., Terlevich R. J., 1998, *MNRAS*, **293**, L49
- Brandl B. R., et al., 2006, *ApJ*, **653**, 1129
- Brinchmann J., Charlot S., White S. D. M., Tremonti C., Kauffmann G., Heckman T., Brinkmann J., 2004, *MNRAS*, **351**, 1151
- Calzetti D., Armus L., Bohlin R. C., Kinney A. L., Koornneef J., Storchi-Bergmann T., 2000, *ApJ*, **533**, 682
- Cardamone C. N., Urry C. M., Schawinski K., Treister E., Brammer G., Gawiser E., 2010, *ApJ*, **721**, L38
- Casey C. M., 2012, *MNRAS*, **425**, 3094
- Chapman S. C., Helou G., Lewis G. F., Dale D. A., 2003, *ApJ*, **588**, 186
- Chen B., Dai X., Kochanek C. S., Chartas G., Blackburne J. A., Kozłowski S., 2011, *ApJ*, **740**, L34
- Chen C.-T. J., et al., 2013, *ApJ*, **773**, 3
- Cicone C., et al., 2014, *A&A*, **562**, A21
- Ciesla L., et al., 2014, *A&A*, **543**, A161
- Ciesla L., et al., 2014, preprint, ([arXiv:1402.3597](https://arxiv.org/abs/1402.3597))
- Cortese L., et al., 2012a, *A&A*, **540**, A52
- Cortese L., et al., 2012b, *A&A*, **544**, A101
- Cortese L., et al., 2014, *MNRAS*, **440**, 942
- Croton D. J., et al., 2006, *MNRAS*, **365**, 11
- Dai Y. S., Wilkes B. J., Bergeron J., Omont A., Kuraszekiewicz J., Teplitz H. I., 2015, preprint, ([arXiv:1511.06761](https://arxiv.org/abs/1511.06761))
- Dale D. A., Helou G., 2002, *ApJ*, **576**, 159
- Dale D. A., Helou G., Magdis G. E., Armus L., Díaz-Santos T., Shi Y., 2014, *ApJ*, **784**, 83
- Davies R. I., Müller Sánchez F., Genzel R., Tacconi L. J., Hicks E. K. S., Friedrich S., Sternberg A., 2007, *ApJ*, **671**, 1388
- Devereux N. A., Young J. S., 1990, *ApJ*, **350**, L25
- Diamond-Stanic A. M., Rieke G. H., 2010, *ApJ*, **724**, 140
- Diamond-Stanic A. M., Rieke G. H., 2012, *ApJ*, **746**, 168
- Donley J. L., et al., 2012, *ApJ*, **748**, 142
- Draine B. T., 2003, *ARA&A*, **41**, 241
- Draine B. T., Lee H. M., 1984, *ApJ*, **285**, 89
- Esquej P., et al., 2014, *ApJ*, **780**, 86
- Feigelson E. D., Nelson P. I., 1985, *ApJ*, **293**, 192
- Ferrarese L., Merritt D., 2000, *ApJ*, **539**, L9
- Foreman-Mackey D., Hogg D. W., Lang D., Goodman J., 2013, *PASP*, **125**, 306
- Franceschini A., Hasinger G., Miyaji T., Malquori D., 1999, *MNRAS*, **310**, L5
- Fritz J., Franceschini A., Hatziminaoglou E., 2006, *MNRAS*, **366**, 767
- Gandhi P., Horst H., Smette A., Hönig S., Comastri A., Gilli R., Vignali C., Duschl W., 2009, *A&A*, **502**, 457
- García-González J., et al., 2016, *MNRAS*, **458**, 4512
- Gebhardt K., et al., 2000, *ApJ*, **539**, L13
- Griffin M. J., et al., 2010, *A&A*, **518**, L3
- Gültekin K., et al., 2009, *ApJ*, **698**, 198
- Häring N., Rix H.-W., 2004, *ApJ*, **604**, L89
- Hickox R. C., Mullaney J. R., Alexander D. M., Chen C.-T. J., Civano F. M., Goulding A. D., Hainline K. N., 2014, *ApJ*, **782**, 9
- Hopkins P. F., Quataert E., 2010, *MNRAS*, **407**, 1529
- Kauffmann G., et al., 2003, *MNRAS*, **341**, 54
- Kelly B. C., 2007, *ApJ*, **665**, 1489
- Kennicutt Jr. R. C., 1998, *ARA&A*, **36**, 189
- Kennicutt R. C., Evans N. J., 2012, *ARA&A*, **50**, 531
- Kennicutt R. C., et al., 2011, *PASP*, **123**, 1347
- Kormendy J., Ho L. C., 2013, *ARA&A*, **51**, 511
- Koss M., Mushotzky R., Veilleux S., Winter L. M., Baumgartner W., Tueller J., Gehrels N., Valencic L., 2011, *ApJ*, **739**, 57
- LaMassa S. M., Heckman T. M., Ptak A., Urry C. M., 2013, *ApJ*, **765**, L33
- Lacy M., et al., 2004, *ApJS*, **154**, 166
- Lebouteiller V., Barry D. J., Spoon H. W. W., Bernard-Salas J., Sloan G. C., Houck J. R., Weedman D. W., 2011, *ApJS*, **196**, 8
- Lilly S. J., Carollo C. M., Pipino A., Renzini A., Peng Y., 2013, *ApJ*, **772**, 119
- Lonsdale Persson C. J., Helou G., 1987, *ApJ*, **314**, 513
- Lutz D., Maiolino R., Spoon H. W. W., Moorwood A. F. M., 2004, *A&A*, **418**, 465
- Lutz D., et al., 2008, *ApJ*, **684**, 853
- Magnelli B., et al., 2014, *A&A*, **561**, A86
- Magorrian J., et al., 1998, *AJ*, **115**, 2285
- Marconi A., Hunt L. K., 2003, *ApJ*, **589**, L21
- Martin D. C., et al., 2007, *ApJS*, **173**, 342
- Matsuoka Y., et al., 2015, *ApJ*, **811**, 91
- McConnell N. J., Ma C.-P., 2013, *ApJ*, **764**, 184
- Meléndez M., Mushotzky R. F., Shimizu T. T., Barger A. J., Cowie L. L., 2014, *ApJ*, **794**, 152
- Merloni A., Heinz S., 2013, Evolution of Active Galactic Nuclei. p. 503, [doi:10.1007/978-94-007-5609-0_11](https://arxiv.org/abs/10.1007/978-94-007-5609-0_11)
- Mullaney J. R., Alexander D. M., Goulding A. D., Hickox R. C., 2011, *MNRAS*, **414**, 1082
- Mullaney J. R., et al., 2012, *MNRAS*, **419**, 95
- Mullaney J. R., et al., 2015, *MNRAS*, **453**, L83
- Murphy E. J., et al., 2011, *ApJ*, **737**, 67
- Mushotzky R., 2004, in Barger A. J., ed., *Astrophysics and Space Science Library Vol. 308, Supermassive Black Holes in the Distant Universe*. p. 53 ([arXiv:astro-ph/0405144](https://arxiv.org/abs/astro-ph/0405144))
- Nandra K., et al., 2007, *ApJ*, **660**, L11
- Netzer H., 2009, *MNRAS*, **399**, 1907
- Netzer H., et al., 2007, *ApJ*, **666**, 806
- Noeske K. G., et al., 2007, *ApJ*, **660**, L43
- Page M. J., et al., 2012, *Nature*, **485**, 213
- Peng Y., Maiolino R., Cochrane R., 2015, *Nature*, **521**, 192
- Pilbratt G. L., et al., 2010, *A&A*, **518**, L1
- Poglitsch A., et al., 2010, *A&A*, **518**, L2
- Puget J. L., Leger A., 1989, *ARA&A*, **27**, 161
- Rosario D. J., et al., 2012, *A&A*, **545**, A45

- Roussel H., Sauvage M., Vigroux L., Bosma A., 2001, *A&A*, **372**, 427
- Rovilos E., et al., 2012, *A&A*, **546**, A58
- Salim S., et al., 2007, *ApJS*, **173**, 267
- Sargsyan L. A., Weedman D. W., 2009, *ApJ*, **701**, 1398
- Schawinski K., et al., 2010, *ApJ*, **711**, 284
- Schawinski K., et al., 2014, *MNRAS*, **440**, 889
- Shi Y., Helou G., Armus L., Stierwalt S., Dale D., 2013, *ApJ*, **764**, 28
- Shi Y., Rieke G. H., Ogle P. M., Su K. Y. L., Balog Z., 2014, *ApJS*, **214**, 23
- Shimizu T. T., Mushotzky R. F., Meléndez M., Koss M., Rosario D. J., 2015, *MNRAS*, **452**, 1841
- Shimizu T. T., Meléndez M., Mushotzky R. F., Koss M. J., Barger A. J., Cowie L. L., 2016, *MNRAS*, **456**, 3335
- Shipley H. V., Papovich C., Rieke G. H., Brown M. J. I., Moustakas J., 2016, *ApJ*, **818**, 60
- Silk J., Rees M. J., 1998, *A&A*, **331**, L1
- Silverman J. D., et al., 2008, *ApJ*, **675**, 1025
- Silverman J. D., et al., 2009, *ApJ*, **696**, 396
- Smith J. D. T., et al., 2007, *ApJ*, **656**, 770
- Smith M. W. L., et al., 2012, *ApJ*, **756**, 40
- Spoon H. W. W., Marshall J. A., Houck J. R., Elitzur M., Hao L., Armus L., Brandl B. R., Charmandaris V., 2007, *ApJ*, **654**, L49
- Stanley F., Harrison C. M., Alexander D. M., Swinbank A. M., Aird J. A., Del Moro A., Hickox R. C., Mullaney J. R., 2015, *MNRAS*, **453**, 591
- Stern D., et al., 2012, *ApJ*, **753**, 30
- Stone M., Veilleux S., Melendez M., Sturm E., Gracia-Carpio J., Gonzalez-Alfonso E., 2016, preprint, ([arXiv:1605.06512](https://arxiv.org/abs/1605.06512))
- Symeonidis M., et al., 2013, *MNRAS*, **431**, 2317
- Temi P., Brighenti F., Mathews W. G., 2007, *ApJ*, **660**, 1215
- Thacker R. J., MacMackin C., Wurster J., Hobbs A., 2014, *MNRAS*, **443**, 1125
- Tombesi F., Meléndez M., Veilleux S., Reeves J. N., González-Alfonso E., Reynolds C. S., 2015, *Nature*, **519**, 436
- Treyer M., et al., 2010, *ApJ*, **719**, 1191
- Veilleux S., et al., 2013, *ApJ*, **776**, 27
- Viero M. P., et al., 2014, *ApJS*, **210**, 22
- Vito F., et al., 2014, *MNRAS*, **441**, 1059
- Winter L. M., Veilleux S., McKernan B., Kallman T. R., 2012, *ApJ*, **745**, 107
- Wright E. L., et al., 2010, *AJ*, **140**, 1868
- Wu Y., Charmandaris V., Huang J., Spinoglio L., Tommasin S., 2009, *ApJ*, **701**, 658
- Wuyts S., et al., 2011, *ApJ*, **742**, 96
- Xue Y. Q., et al., 2010, *ApJ*, **720**, 368
- Zibetti S., Charlot S., Rix H.-W., 2009, *MNRAS*, **400**, 1181
- da Cunha E., Emission C., Charlot S., Blaizot J., 2010, *MNRAS*, **403**, 1894

APPENDIX A: SED PARAMETER ESTIMATION

To find the best fitting parameters in our SED modeling, instead of standard least squares analysis, we used a Bayesian framework along with Monte Carlo Markov Chains to probe the posterior probability distribution functions for each parameter. The Bayesian framework allows for robust estimates of the uncertainty and for explicit statements about prior knowledge of the parameters. It also makes it relatively easy to include information contained in the undetected photometry of the SED.

A1 Likelihood Representation

The likelihood defines the probability of observing a set of data given a specific model. In SED fitting, this translates to the combined probability of measuring all the photometric data points in the observed SED given a model for the SED (whether based on templates or analytic models). The total likelihood can then be expressed as the product of the probabilities of observing each single photometric point:

$$\mathcal{L}(F|M) = \prod_i P(F_i|M) \quad (\text{A1})$$

where F is the set of photometric fluxes, F_i and M is the model. For our analysis, we assume the probability of our observations follows a Gaussian distribution with mean equal to M and standard deviations equal to the measurement errors, σ_i .

$$P(F_i|M) = \frac{1}{\sqrt{2\pi\sigma_i^2}} \exp\left(-\frac{(F_i - M)^2}{2\sigma_i^2}\right) \quad (\text{A2})$$

Equation A2 only defines the probability for detected fluxes. To use the information contained in the undetected photometry, U_i , we define a different probability under the assumption that all of the upper limits are 5σ .

$$\begin{aligned} P(U_i|M) &= \int_{-\infty}^{U_i} \frac{1}{\sqrt{2\pi\sigma_i^2}} \exp\left(-\frac{(x - M)^2}{2\sigma_i^2}\right) dx \\ &= \frac{1}{2} \left(1 + \operatorname{erf}\left[\frac{U_i - M}{\sigma_i \sqrt{2}}\right]\right) \end{aligned} \quad (\text{A3})$$

where $\sigma_i = \frac{U_i}{5}$ and erf is the standard error function. For numerical accuracy and simplicity, it is customary to minimize the negative log-likelihood. Supposing we have N total SED points with D detections and $D - N$ non-detections then the total negative log-likelihood combining Equations A1, A2, and A3 is:

$$\begin{aligned} -\log \mathcal{L} &= \frac{1}{2} \sum_{i=0}^D \left[\log(2\pi\sigma_i^2) - \left(\frac{F_i - M}{\sigma_i}\right)^2 \right] + \\ &\quad \sum_{j=0}^{D-N} \log \left[1 + \operatorname{erf}\left(\frac{U_j - M}{\sigma_j \sqrt{2}}\right) \right] \end{aligned} \quad (\text{A4})$$

It is important to recognize here how M is calculated, no matter whether it represents a template or analytic model. Each data point in an SED is the observer-frame flux density measured over a defined wavelength range. Therefore, to determine the model flux densities we first redshifted the full rest-frame model SED into the observer frame using the known redshifts of all of our sources. This observer-frame SED was then convolved with each instrument filter transmission curve to produce model flux densities that can be accurately compared to the observed ones.

A2 Bayesian MCMC Analysis

Within the Bayesian framework, the important probability is the probability of the model given the data at hand, i.e.

the most probable SED model given the observed fluxes. This probability can be determined using Bayes theorem:

$$P(M|F) = \frac{P(F|M)P(M)}{P(F)} \quad (\text{A5})$$

and is known as the posterior probability distribution. $P(F|M)$ is proportional to the likelihood (Equation A1), $P(M)$ codifies our prior knowledge about the model, and $P(F)$ is the model evidence and can be disregarded as a simple normalization term.

The reader may notice that assuming a flat prior, $P(M) \propto 1$, reduces Equation A5 to $P(M|F) \propto \mathcal{L}$ verifying our use of maximum likelihood in determining the best template models.

For the C12 model, we used flat priors for the dust temperature and dust mass. We placed conservative limits on both the dust temperature and $\log M_{\text{dust}}$ to be between 1 and 100 K and 1 and 10 M_{\odot} respectively. Within the power-law component for the C12 model, we also used flat priors for the powerlaw slope between -5 and 5 and the log of the normalization between -10 and 10. Based on previous work attempting to measure the intrinsic AGN SED and modeling the dusty torus, we expect the SED to turnover anywhere in the range between 20-70 μm . Therefore we imposed a Gaussian prior centered at 45 μm with a standard deviation of 20 μm . We found that imposing this prior resulted in better and more realistic fits to the SEDs.

We used the PYTHON package EMCEE (Foreman-Mackey et al. 2013) to perform MCMC and sample the posterior probability distribution function (Equation A5). EMCEE runs an implementation of the Affine-Invariant MCMC sampler from Goodman & Weare 2010. Instead of one single MCMC chain, it samples the posterior PDF with multiple “walkers”, each with their own chain. For our analysis, we used 50 walkers that each produced a 1000 step chain. To allow for each chain to stabilize and move away from the initial guesses for the parameters, we imposed a 200 step “burn-in”. In total, this resulted in 40000 steps to define the full posterior PDF.

To determine the best fit parameters, we first marginalized the posterior PDF over all other parameters and then calculated the median. All quoted uncertainties represent the 68% confidence interval determined from the 16th and 84th percentile of the marginalized posterior PDF.

For sources with less than four detections in their SED, we fixed the dust temperature to 25 K since the peak of the FIR bump is no longer constrained. In these cases, we only obtained upper limits on the dust mass by calculating the upper 95th percentile of the marginalized PDF.

APPENDIX B: COMPARISON BETWEEN DIFFERENT MODELS

In this section we compare the results for the total luminosity, IR AGN luminosity, and star forming luminosity between the C12 model and two other models to decompose the SED. We exclude from this analysis objects which were only detected by *Herschel* a less than one waveband given the strong uncertainties associated with their properties. We also exclude as before the 6 radio-loud objects and Mrk 3 (for lack of WISE data).

B1 DecompIR model

Besides analytic models, another popular method is the use of template SEDs. Templates are constructed based on well-sampled SEDs of large samples of galaxies and usually parameterized according to a known property such as infrared luminosity.

For galaxies known to host an AGN, recent studies have turned to the DECOMP-IR (Mullaney et al. 2011) templates. DECOMP-IR consists of five host galaxy templates that span the IR color and luminosity range of the original Brandl et al. (2006) starburst galaxy templates. Mullaney et al. (2011) constructed the AGN templates based on a subsample of the *Swift*/BAT AGN which had AGN dominated *Spitzer*/IRS spectra determined by the equivalent width of the 11.3 μm feature being $< 0.03 \mu\text{m}$. The *Spitzer*/IRS spectra were combined with *IRAS* photometry at 60 and 100 μm to define the “intrinsic” AGN SED from 6–100 μm .

Mullaney et al. (2011) created three different AGN templates: one based only on high AGN luminosity objects, low AGN luminosity objects, and a median of the entire sample. For this work, we only consider the median AGN template given our SEDs only contain two points in the MIR where AGN-related emission is expected to dominate.

B2 Dale et al 2014 model

The third model we chose to test on our sample is the semi-empirical templates from Dale et al. (2014, hereafter D14). These templates also contain two components, one for dust emission in the host galaxy and one for the AGN. The host galaxy components were built from an updated version of the Dale & Helou (2002) model. Each component represents an SED produced using a different value of α_{SF} , which is the powerlaw slope of the intensity distribution for the interstellar radiation field that is heating the dust. These SEDs contain a mixture of emission from PAHs, small stochastically heated grains, and thermally radiating large grains.

For the AGN component, D14 chose the median SED of the Palomar-Green quasars from Shi et al. (2013) citing the care with which any star-forming component was removed and the prominence of several AGN related MIR features such as the [OIV] fine structure line and the broad 10 and 18 μm silicate emission bumps. At long wavelengths the AGN template falls as a blackbody.

Instead of two separate templates for the AGN and host galaxy, D14 provided a single set of templates based on different combinations of α_{SF} and f_{AGN} , the fractional contribution of the AGN to the 5–20 μm emission. In total there are 1365 templates that range in $\alpha_{\text{SF}} = 0.0625 - 4.0$ in 0.0625 intervals and $f_{\text{AGN}} = 0 - 1$ in 0.05 intervals.

B3 SED Fitting for the template models

For each template in a model set, Equation A4 was minimized to determine the best fit normalization. We then chose the normalized template with the lowest $-\log \mathcal{L}$ as the best fitting model for a source. For the DecompIR set, this meant first simultaneously optimizing over a normalization for the AGN component and each host galaxy component, then choosing the combined template that resulted in the

minimum $-\log \mathcal{L}$. For D14, this meant calculating $-\log \mathcal{L}$ over the entire set of α and f_{AGN} templates.

Uncertainties using the maximum likelihood method were determined by generating 1000 simulated SEDs for each source. These data points in the simulated SEDs were calculated by assuming each detected point followed a Gaussian distribution with mean equal to the observed flux density and a standard deviation equal to the measured error. Each of the simulated SEDs were re-fit using the same method. The standard deviation on the set of best fit parameters from the simulated SEDs then was used as the uncertainty. In this way both statistical and systematic errors can be taken into account in assessing the reliability of our best fit parameters.

B4 L_{IR} Comparison

The measured property that should be most model independent is the total infrared luminosity, L_{IR} . Assuming each model was able to fit well the broadband SEDs and reproduce the observed photometry, L_{IR} is simply the total integrated energy underneath the SED, irregardless of how the SED is decomposed. In Figure B1, we plot the correlations between the C12 model and DecompIR and D14 models for L_{IR} .

The median $\log L_{\text{IR}}$ for the C12, DecompIR, and D14 models are all $10.39 L_{\odot}$ with a spread of 0.5 dex. Clearly, based on Figure B1, each model well fits the broadband SED of our sample with a small scatter around the 1-to-1 correspondence line. The average difference in the luminosities from each model is only ~ 0.01 dex with a standard deviation between 0.05 and 0.08 dex, slightly higher than the median statistical uncertainty for the C12 model of 0.03 dex.

B5 L_{SF} , $L_{\text{AGN,IR}}$, and f_{AGN} Comparison

Where the models begin to disagree more, is in the actual decomposition of the SED. In particular, we compare L_{SF} , $L_{\text{AGN,IR}}$, and f_{AGN} . Calculating these parameters for the template models is relatively easy compared to the corrections we had to make for the C12 model. For the DecompIR template set, L_{IR} , L_{SF} , and $L_{\text{AGN,IR}}$ were simply calculated from the best fit total, host galaxy, and AGN SEDs. For the D14 model set, L_{IR} was measured from the best fitting template and L_{SF} and $L_{\text{AGN,IR}}$ were calculated based on the best fit f_{AGN} .⁷ Uncertainties on all of these luminosities were determined with the same Monte Carlo method used to determine the uncertainties on the best fitting parameters.

Figures B2, B3, and B4 display the relationship between each model's L_{SF} , $L_{\text{AGN,IR}}$, and f_{AGN} . Out of the three parameters, L_{SF} is most consistent between the three models. The C12, DecompIR, and D14 models have a median L_{SF} of 10.12, 10.12, and 10.19 L_{\odot} respectively. The average difference between C12 and DecompIR is only 0.006 dex with a standard deviation of 0.16 dex while the average difference between C12 and D14 is -0.07 dex with a standard deviation

of 0.11 dex. The DecompIR and D14 are measuring slightly higher star-forming luminosities. Based on these differences, we assign a conservative uncertainty of 0.2 dex for L_{SF} to account for model dependence.

The comparison for $L_{\text{AGN,IR}}$ shows increased scatter compared to the two previous luminosities. The median $L_{\text{AGN,IR}}$ for the three models is 10.04, 9.9, and 9.85 L_{\odot} for the C12, DecompIR, and D14 models respectively. The average difference between C12 and DecompIR is 0.10 dex with a standard deviation of 0.20 dex while the average difference between C12 and D14 is 0.14 dex with a standard deviation of 0.20 dex. Since the DecompIR and D14 were measuring higher L_{SF} , it makes sense that they are measuring lower $L_{\text{AGN,IR}}$ given the total infrared luminosities between the three models was identical. It is likely that the more flexible C12 model which allows the PL component to extend to longer wavelengths creates the discrepancy between it and the template based models. Our implementation of DecompIR and D14 adheres to a strict single template for the intrinsic AGN SED. Adding the offset and spread in the differences in quadrature indicates an uncertainty of 0.25 dex in the determination of $L_{\text{AGN,IR}}$.

The relatively large uncertainty in $L_{\text{AGN,IR}}$ then leads to a large scatter in f_{AGN} as shown in Figure B4. The average difference between C12 and DecompIR is only 0.02 however the standard deviation is 0.13. The average difference between C12 and D14 is 0.1 with a standard deviation of 0.11. Given the spread in f_{AGN} is comparable to the average statistical uncertainty (0.14) from our C12 modeling, we do not add any more uncertainty onto our estimates.

The 15 per cent uncertainty between the three models represents our general lack of knowledge about the details of decomposing broadband SEDs of AGN host galaxies. The estimated f_{AGN} is highly dependent on the assumed models of both the host galaxy and AGN, and currently at best we can only constrain to within 15 per cent. This influences then the calculations of both the SFR (based on L_{SF}) and the IR portion of AGN luminosity ($L_{\text{AGN,IR}}$). Studies relying on calculating the SFR of AGN host galaxies using the infrared need to take these discrepancies into account or else risk over-interpreting results based on broad SED decomposition. This also highlights the need for high angular resolution studies of AGN, to determine the true shape of the AGN IR SED.

APPENDIX C: COMPARISON OF L_{SF} WITH PAH MEASUREMENTS

To test our estimates of the star-forming luminosity (L_{SF}), we compare them with estimates of the star-forming luminosity calculated from the PAH 11.3 and 7.7 μm luminosity. PAH features are thought to be caused by the vibrations of complex hydrocarbons (Draine & Lee 1984; Puget & Leger 1989) and have been shown to be reliable tracers of the SFR (Roussel et al. 2001; Sargsyan & Weedman 2009; Treyer et al. 2010; Shipley et al. 2016) even for AGN (Diamond-Stanic & Rieke 2010). Therefore, comparing our L_{SF} with the 11.3 and 7.7 μm PAH luminosity provides a further check on our SED decomposition.

To measure the 7.7 and 11.3 μm luminosities we first searched the Cornell Atlas of Spitzer IRS Sources

⁷ Dale et al. (2014) only provides f_{AGN} calculated between 5–15 μm , however D. Dale graciously provided the authors with f_{AGN} calculated between 8–1000 μm through private communication in August 2015.

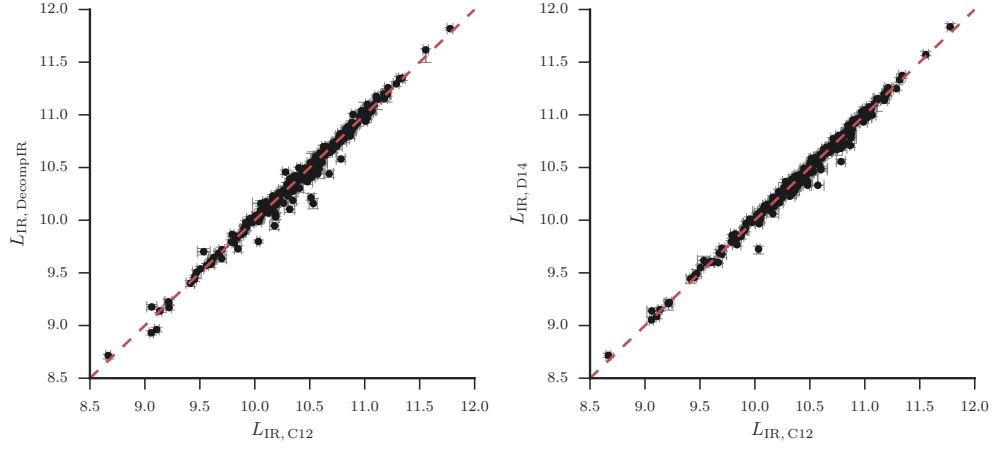


Figure B1. Correlations of total L_{IR} between the C12 model and DecompIR and D14. The red dashed line indicates a 1-to-1 correspondence.

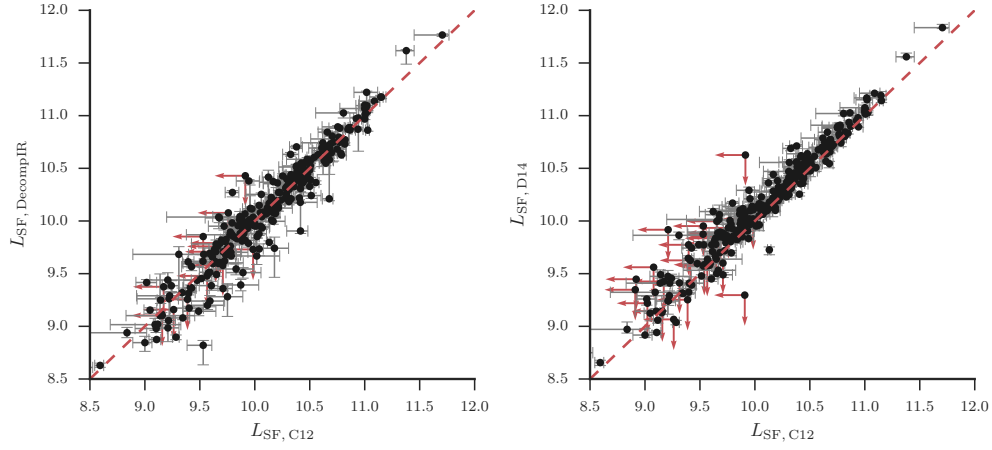


Figure B2. Same as Figure B1 but for L_{SF}

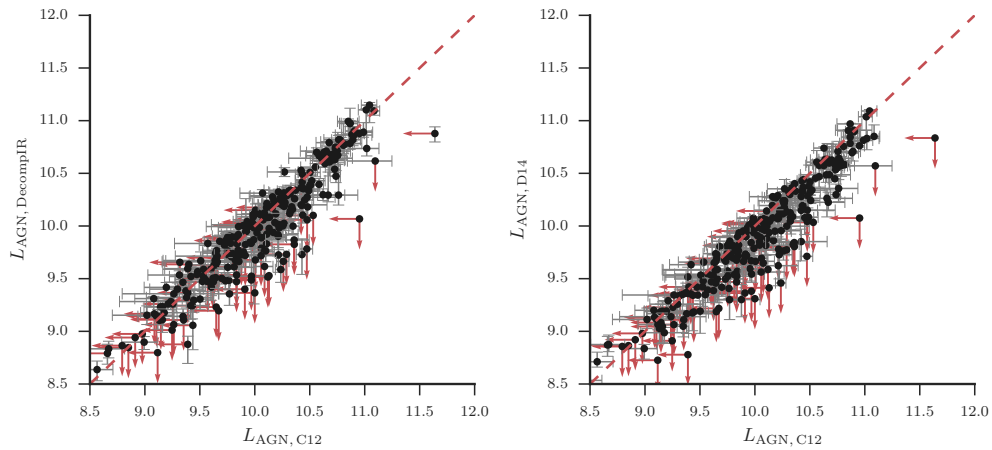


Figure B3. Same as Figure B1 but for $L_{\text{AGN,IR}}$

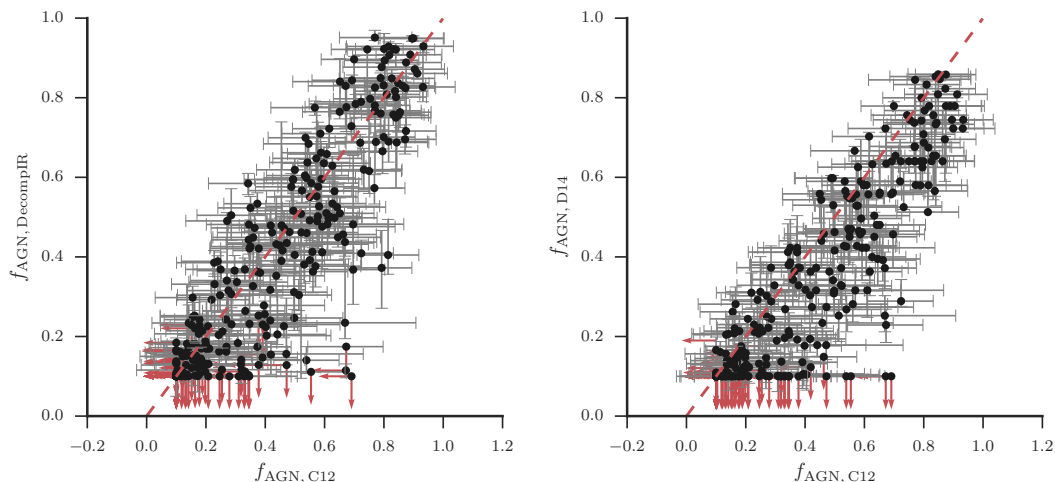


Figure B4. Correlations of f_{AGN} from the three SED models. Error bars represent the 68% confidence interval. Upper limits are indicated as red downward pointing arrows. The red dashed line indicates a 1-to-1 correspondence. A color version of this figure is available in the online publication.

(Lebouteiller et al. 2011, CASSIS;) for low-resolution Spitzer/IRS spectra of the *Herschel*-BAT AGN. We found 120/313 AGN on CASSIS and downloaded their reduced spectra using the default extraction method. Due to the different sizes of the Short-Low (SL) slit and Long-Low (LL) slit, the continuum of each can be offset mainly from extended emission not captured by the SL slit. Therefore spectral orders were stitched together by fitting a line to the ends of each order and scaling to match the overlapping regions. SL2 and LL2 were first matched and scaled to SL1 and LL1 respectively. Then the combined SL1/SL2 spectra was matched to the combined LL1/LL2 spectra to produce the final full Spitzer/IRS low resolution spectra.

We fit each spectra using small spectral windows centered on 7.7 and 11.3 μm . Following Smith et al. (2007) and the popular spectral fitting software package, PAHFIT, we modeled the PAH features using a Drude profile and any emission lines contained in the spectral windows as narrow Gaussians. The full-width-at-half-maximum (FWHM) and central wavelength of the emission lines were kept fixed at the values in Table 2 of Smith et al. (2007). The 7.7 and 11.3 μm features are actually complexes with multiple sub-features. PAHFIT models these with multiple Drude profiles chosen to reproduce the observed features and we follow this method using the values for the fractional contribution and FWHM as given in Table 3 of Smith et al. (2007). We model the continuum as a simple third-order polynomial. This allows the continuum to take on many shapes that is more necessary for AGN spectra which can show broad silicate absorption and emission and varying continuum slopes (Baum et al. 2010; Spoon et al. 2007; Wu et al. 2009). While silicate absorption is included within PAHFIT, silicate emission is absent prompting the need for own modeling. Finally, to determine the best-fit model, we again use the Bayesian methodology and MCMC described in Appendix A. This allows us to treat the continuum and other nearby features as nuisance parameters and robustly determine uncertainties on the 7.7 and 11.3 μm luminosities.

Figure C1 shows the correlation between L_{SF} and L_{PAH}

for both the 7.7 (right) and 11.3 μm (left) complexes. We chose to use the KINGFISH galaxies (red squares) as a comparison here rather than HRS given the readily available PAH measurements. L_{SF} was determined using the C12 model in the same way as the HRS sample and L_{PAH} is from Smith et al. (2007). The L_{PAH} for KINGFISH were measured using PAHFIT, but given the large similarity with our method, we do not expect large differences.

Based on Figure C1, both the KINGFISH and *Herschel*-BAT samples seem to follow broadly the same correlation indicating we are neither over nor under estimating L_{SF} from our SED decomposition for the *Herschel*-BAT AGN. Using LINMIX, we measured the relationship for both samples and both PAH luminosities. The median correlations with 95% confidence intervals are shown in Figure C1 with the blue and red solid lines and shaded regions corresponding to the *Herschel*-BAT AGN and KINGFISH samples respectively. For the *Herschel*-BAT AGN we find slopes of 1.26 ± 0.1 (11.3 μm) and 1.32 ± 0.11 (7.7 μm) while for the KINGFISH galaxies we find slopes of 1.02 ± 0.15 and 1.11 ± 0.16 . The *Herschel*-BAT AGN show a slightly steeper relationship than the KINGFISH galaxies, however they are still within $\sim 1.5\sigma$ of each other. The steepness of the correlation for the *Herschel*-BAT AGN could be driven by the large number of upper limits for the PAH luminosities. Indeed, when excluding these from the analysis we find slopes of 1.13 ± 0.09 and 1.15 ± 0.12 , much closer to the KINGFISH galaxies.

For the purposes of this work, Figure C1 indicates that our SED decomposition of the *Herschel*-BAT AGN has produced reliable estimates of the star-forming luminosity consistent with measurements of the PAH 11.3 and 7.7 μm luminosity. A more detailed analysis on the exact correlation between broadband IR luminosity and PAH emission for AGN is beyond the scope of this Paper and has no bearing on our results.

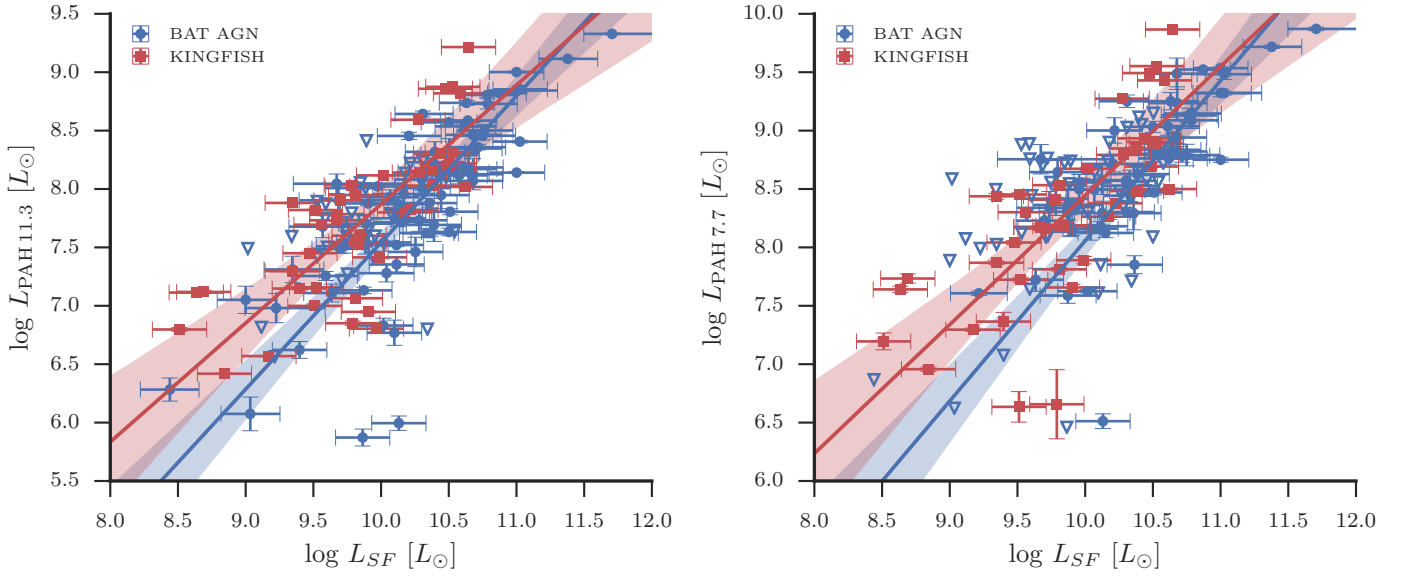


Figure C1. Correlation between L_{SF} and the 11.3 (left) and 7.7 μm (right) luminosity. Blue points correspond to the *Herschel*-BAT AGN and red squares correspond to the KINGFISH galaxies. Sources with upper limits on L_{PAH} are shown as open triangles. Measured correlations between L_{SF} and the 11.3 and 7.7 μm luminosity are shown as solid blue and red lines for the *Herschel*-BAT AGN and KINGFISH samples respectively. The shaded region around the median correlations indicate the 95% confidence interval. The broad consistency of the correlation for both the KINGFISH and *Herschel*-BAT samples shows that SFRs determined from L_{SF} will be comparable without any systematic bias.

APPENDIX D: SED FIGURES

This paper has been typeset from a \LaTeX file prepared by the author.

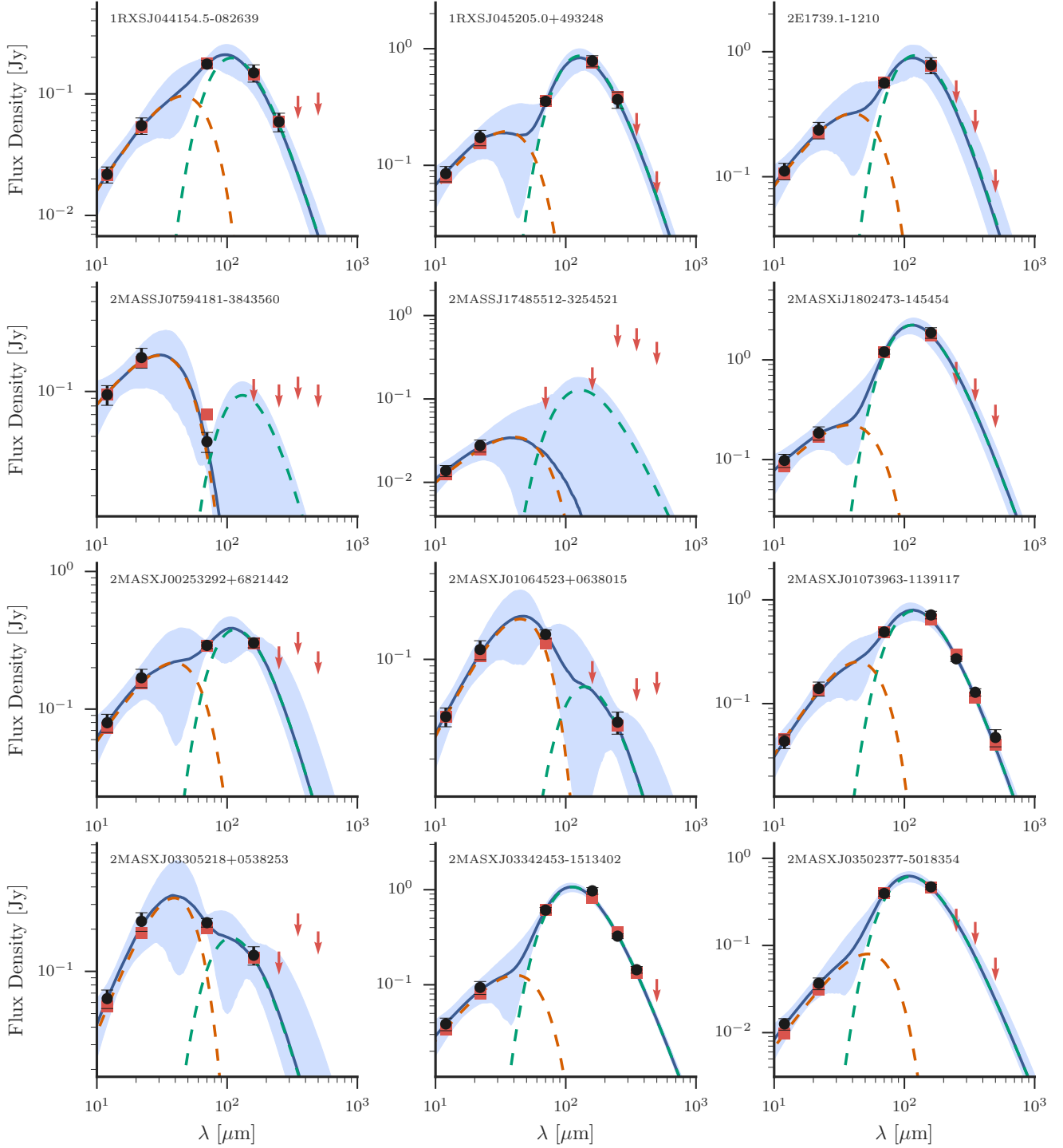


Figure D1. Observed frame 12–500 μm SEDs for all of the *Herschel*-BAT sample. Black points plot the observed flux densities with downward-pointing red arrows indicating 5σ upper limits. The solid blue line and shaded region shows the best-fit C12 model with a 95 percent confidence interval. The red squares are the model flux densities after convolving the best-fit model SED with each instrument's transmission curve. The orange and green dashed lines show the best-fit PL and MBB components, respectively.